Mutations affecting the actin regulator WD repeat–containing protein 1 lead to aberrant lymphoid immunity
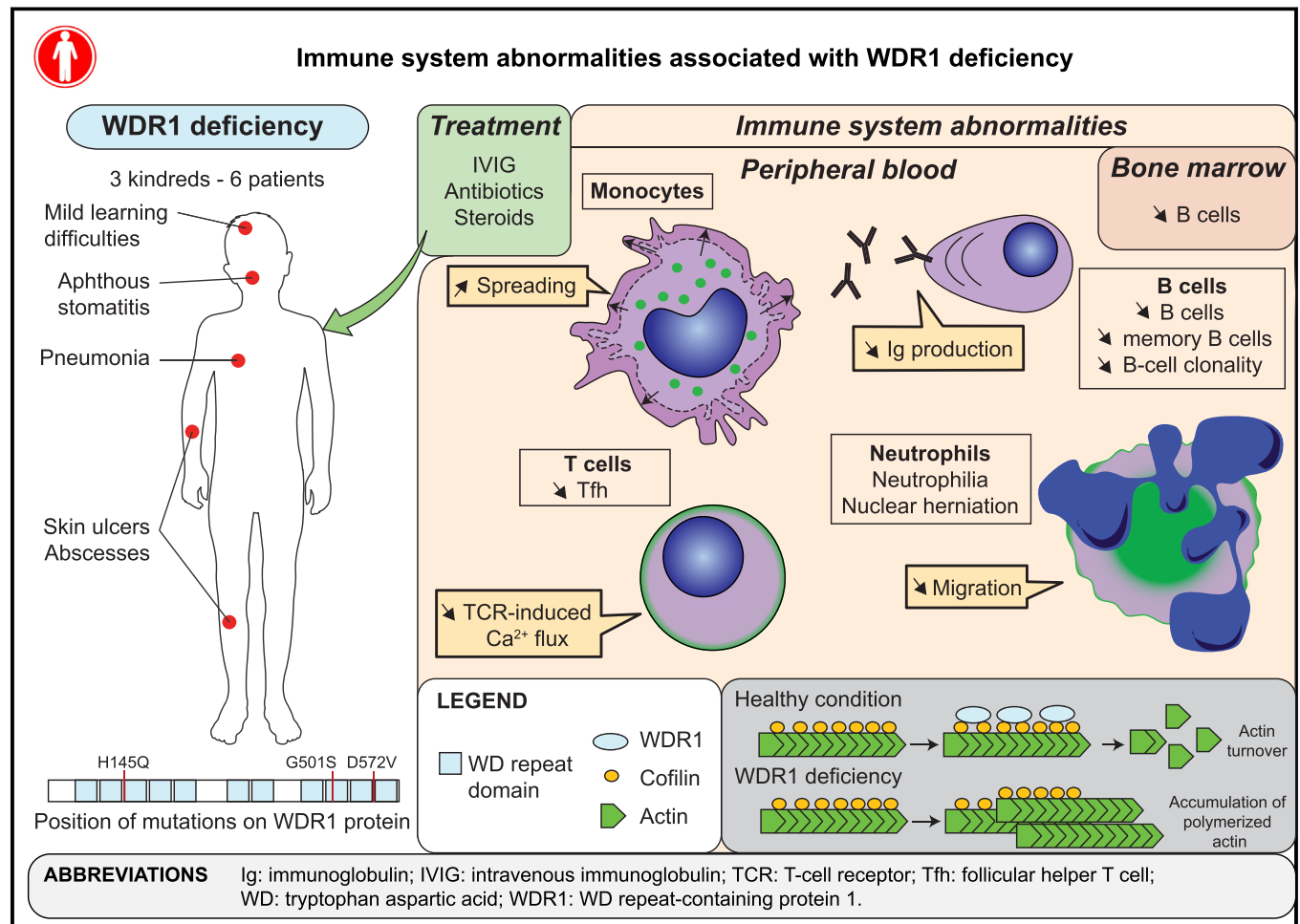
Laurène Pfajfer, MSc,[a,b,c,d,e]* Nina K. Mair, BSc,[a,b]* Raúl Jiménez-Heredia, MSc,[a,b] Ferah Genel, MD,[f]
Nesrin Gulez, MD,[f] Ömür Ardeniz, MD,[g] Birgit Hoeger, PhD,[a,b] Sevgi Köstel Bal, MD, PhD,[a,b,h]
Christoph Madritsch, PhD,[i] Artem Kalinichenko, PhD,[a,b] Rico Chandra Ardy, MSc,[a,b] Bengü Gerçeker, MD,[j]
Javier Rey-Barroso, PhD,[c,d,e] Hanna Ijspeert, PhD,[k] Stuart G. Tangye, PhD,[l,m] Ingrid Simonitsch-Klupp, MD,[n]
Johannes B. Huppa, PhD,[i] Mirjam van der Burg, PhD,[k] Loïc Dupré, PhD,[a,b,c,d,e]‡ and Kaan Boztug, MD[a,b,o,p]‡

Vienna, Austria, Toulouse, France, Izmir and Ankara, Turkey, Rotterdam, The Netherlands, and Darlinghurst, Australia

GRAPHICAL ABSTRACT

Immune system abnormalities associated with WDR1 deficiency

1

Background: The actin-interacting protein WD repeat–containing protein 1 (WDR1) promotes cofilin-dependent actin filament turnover. Biallelic *WDR1* mutations have been identified recently in an immunodeficiency/autoinflammatory syndrome with aberrant morphology and function of myeloid cells.

Objective: Given the pleiotropic expression of WDR1, here we investigated to what extent it might control the lymphoid arm of the immune system in human subjects.

Methods: Histologic and detailed immunologic analyses were performed to elucidate the role of WDR1 in the development and function of B and T lymphocytes.

Results: Here we identified novel homozygous and compound heterozygous *WDR1* missense mutations in 6 patients belonging to 3 kindreds who presented with respiratory tract infections, skin ulceration, and stomatitis. In addition to defective adhesion and motility of neutrophils and monocytes, WDR1 deficiency was associated with aberrant T-cell activation and B-cell development. T lymphocytes appeared to develop normally in the patients, except for the follicular helper T-cell subset. However, peripheral T cells from the patients accumulated atypical actin structures at the immunologic synapse and displayed reduced calcium flux and mildly impaired proliferation on T-cell receptor stimulation. WDR1 deficiency was associated with even more severe abnormalities of the B-cell compartment, including peripheral B-cell lymphopenia, paucity of B-cell progenitors in the bone marrow, lack of switched memory B cells, reduced clonal diversity, abnormal B-cell spreading, and increased apoptosis on B-cell receptor/Toll-like receptor stimulation.

Conclusion: Our study identifies a novel role for WDR1 in adaptive immunity, highlighting WDR1 as a central regulator of actin turnover during formation of the B-cell and T-cell immunologic synapses. (J Allergy Clin Immunol 2018;■■■:■■■-■■■.)

Key words: WD repeat–containing protein 1, actin cytoskeleton, immunodeficiency, lymphocytes, immunologic synapse

Actin cytoskeletal dynamics drive a wide array of cellular processes, such as morphogenesis, polarity, and motility.[1] Actin regulators work in concert to tune the assembly and turnover of actin filament meshworks at different cellular locations.[2] Immune cell function relies on finely tuned actin cytoskeletal dynamics. Indeed, both myeloid and lymphoid cells are highly motile and need to establish dynamic cell-to-cell contacts to execute their function. The pivotal role of the actin cytoskeleton in driving immune cell function in human subjects is being revealed by the characterization of a growing number of inherited defects of the immune system (primary immunodeficiencies [PIDs]) caused by deficiency or molecular alteration of actin cytoskeleton–remodeling proteins.[3]

Abbreviations used

APC:	Allophycocyanin
BCR:	B-cell receptor
B-LCL:	EBV-immortalized B-lymphoblastic cell line
CADD:	Combined annotation-dependent depletion
CDR:	Complementarity-determining region
FITC:	Fluorescein isothiocyanate
fMLP:	N-formyl-methionyl-leucyl-phenylalanine
ICAM-1:	Intercellular adhesion molecule 1
IRM:	Interference reflection microscopy
PE:	Phycoerythrin
PID:	Primary immunodeficiency
SHM:	Somatic hypermutation
SLB:	Supported lipid bilayer
TCR:	T-cell receptor
Tfh:	Follicular helper T
TIRF:	Total internal reflection fluorescence
TLR:	Toll-like receptor
WAS:	Wiskott-Aldrich syndrome
WASP:	Wiskott-Aldrich syndrome protein
WDR1:	WD repeat–containing protein 1

A very recently discovered actin-related PID is caused by biallelic loss-of-function mutations in the gene encoding actin-interacting protein 1 (AIP1)/WD repeat–containing protein 1 (WDR1).[4,5] WDR1 is part of a large family of WD (tryptophan-aspartic acid) repeat domain–containing proteins that act as molecular scaffolds through a 7-bladed beta-propeller.[6] WDR1 is expressed ubiquitously and promotes actin filament disassembly through cofilin.[7-12] More precisely, actin filament disassembly relies on sequential recruitment of coronin, cofilin, and WDR1, which act in concert to sever actin filaments.[13-15] WDR1 activity is enhanced further by interaction with the immunomodulatory protease caspase-11.[16]

In human subjects defective expression of WDR1 has been shown recently to affect in particular the innate arm of the immune system. A first study reported 4 children carrying *WDR1* biallelic mutations resulting in severe immunodeficiency associated with a prominent defect in neutrophils, which emitted nuclear herniations and were defective in migrating toward the bacterial chemotactic peptide N-formyl-methionyl-leucyl-phenylalanine (fMLP).[4] A second study reported 2 siblings carrying a *WDR1* biallelic mutation associated with autoinflammation, immunodeficiency, and thrombocytopenia.[5] Expression of misfolded WDR1 in monocyte-derived dendritic cells from those patients led to enlarged actin-rich podosomes and excessive amounts of IL-18 caused by abnormal inflammasome activation. This phenotype is in line with a previous study showing that a hypomorphic mutation

of *Wdr1* in mice results in macrothrombocytopenia and autoinflammatory disease characterized by excessive neutrophil recruitment to sites of inflammation.[17] In these mice neutrophils show increased levels of F-actin and cofilin, resulting in mislocalization and reduced migration.[17] Additional studies have linked aberrant expression of WDR1 in human subjects to gout,[18] pancreatitis,[19] and primary glioblastoma.[20] The extent to which naturally occurring *WDR1* mutations also affect the adaptive arm of the human immune system has not been investigated.

Here we identified the largest cohort of patients with biallelic *WDR1* mutations to date and set out to systematically dissect the consequences on different leukocyte subsets, with a particular focus on lymphocytes.

METHODS
Study oversight

The studies, including immunologic diagnostic procedures and genetic analyses, were performed in accordance with guidelines of good clinical practice, the current version of the Declaration of Helsinki, written informed consent from the patients or patient's legal representatives, and approval from the relevant institutional review boards.

Whole-exome sequencing

For whole-exome sequencing, a TrueSeq Rapid Exome kit, as well as the Illumina HiSeq3000 system and cBot Cluster Generation instruments (Illumina, San Diego, Calif), were used, as previously described,[21,22] with minor changes. Briefly, reads were aligned to the human genome version 19 by using the Burrows-Wheeler Aligner. Variant Effect Predictor was used for annotating single nucleotide variants and insertion/deletion lists. The obtained list was then filtered, excluding variants with a minor allele frequency of greater than 0.01 in the 1000 Genomes, Exome Aggregation Consortium, or dbSNP build 149 databases. After further filtering steps for nonsense, missense, and splice-site variants, an internal database was used to filter for recurrent variants. Moreover, variants are prioritized by using tools, such as SIFT, Polyphen-2, and the combined annotation-dependent depletion (CADD) score,[23] that predict the deleteriousness of a present variant.

Homozygosity mapping

Homozygous sections are mapped with H3M2 (Homozygosity Heterogeneous Hidden Markov Model) software,[24] allowing screening for variants segregating with patient phenotype.

Sanger sequencing

Sanger sequencing was used to validate the *WDR1* variants c.C435G (H145Q) in exon 5 and c.A1715T (D572V) in exon 15 obtained from whole-exome sequencing in the affected family members. Variants in family 3 (D572V in exon 15 and G501S in exon 13) were obtained from direct Sanger sequencing. This was done by designing specific primers for all the variants found: for H145Q in introns 4 and 5 and exon 5/introns 5 and 6, 5'-GTTCTTGGGTCCTTTGGAC -3' (F1) and 5'- CACTTACGCCAATTGT-GAACT -3' (R1); for D572V in introns 14 and 15 and the 3' untranslated region, 5'- CTAGTCCCTGATTCGGTCCA -3' (F2) and 5'- CAGGAGTGT CACGTGGAGAA -3' (R2); and for c.G1501A (G501S) in introns 12 and 13 and introns 13 and 14, 5'- AGGATGGGTGTGGTGTGTG -3' (F3) and 5'- ACAGATAACCTCCCACTGCC -3' (R2).

WDR1 expression

Patient and healthy donor PBMCs were lysed in 100 μL RIPA buffer (150 mmol/L NaCl, 1% Triton X-100, 0.5% sodium deoxycholate, 0.1% SDS, and 50 mmol/L TRIS [pH 8.0]), run on a 10% acrylamide gel at 120 V, and blotted overnight at 120 mA at 4°C on a polyvinylidene difluoride membrane.

Membranes were incubated with anti-human WDR1 (Novus Biologicals, Littleton, Colo) polyclonal antibody at a dilution of 1:600 in Tris-buffered saline with 0.5% Tween and 5% milk overnight at 4°C and a secondary anti-rabbit antibody at room temperature for 2 hours. As a control, glyceraldehyde-3-phosphate dehydrogenase (clone 86C5; Santa Cruz Biotechnology, Dallas, Tex) at a dilution of 1:1000 in combination with a secondary horseradish peroxidase–conjugated goat anti-mouse antibody diluted 1:30,000 was used. Blots were developed with ECL (GE Healthcare, Fairfield, Conn).

Immunophenotyping

Healthy donor and patient PBMCs were obtained by using Ficoll density centrifugation and stained for 30 minutes at 4°C with the following mouse anti-human antibodies: CXCR5–allophycocyanin (APC; 51505) from R&D Systems (Minneapolis, Minn); CCR7–phycoerythrin (PE)-CF594 (150503), CD27 V450 (M-T271), CD27 Brilliant Violet (M-T271), CD38–PE-Cy7 (HIT2), CD21-PE (B-ly4), CD3–APC-H7 (SK7), CD5–Alexa Fluor 700 (UCHT), CD4-APC (RPA-T4), CD4–Brilliant Violet 605 (RPA-T4), CD45RA–Alexa Fluor 700 (HI100), CD8-V500 (RPA-T8), CD8–fluorescein isothiocyanate (FITC; HIT8a), IgM-APC (G20-1273), IgD-FITC (IA6-2), and CD95–PE-Cy7 (DX2) from BD PharMingen (San Jose, Calif); CD19–peridinin-chlorophyll-protein complex-Cy5.5 (HIB19), CD10-APC (CB-CALLA), and CD31-APC (WM59) from eBioscience (San Diego, Calif); CD14–PE-Cy7 (RMO52), CD56-PE (N901), CD4-PE (13B8.2), T-cell receptor (TCR)–Vβ11-FITC (C21), and TCR-Vα24–PC-7 (C15) from Beckman Coulter; and CD8-V450 (RPA-T8) from BD Horizon (BD Biosciences, Franklin Lakes, NJ). Stained cells were analyzed on a BD LSR Fortessa cytometer. Data were processed with FlowJo X software (TreeStar, Ashland, Ore) and sketched with Prism 6.0 software (GraphPad Software, La Jolla, Calif).

Confocal microscopy

On isolation from peripheral blood samples, neutrophils, monocytes, and T cells were transferred onto glass slides precoated with 2 μg/mL fibronectin (all cells) or 10 μg/mL anti-CD3 mAbs (T cells). Neutrophils were stimulated in parallel with 10 nmol/L fMLP, whereas monocytes were treated with 50 ng/mL LPS. After 1 hour of incubation at 37°C, cells were fixed with PFA 3% and stained with Phalloidin–Alexa Fluor 488 (1:40 dilution) for 1 hour in permeabilization buffer (eBioscience) at room temperature in the dark. Slides were imaged with a Zeiss LSM700 confocal microscope (Zeiss, Oberkochen, Germany). The acquired images were analyzed with the ImageJ software (National Institutes of Health, Bethesda, Md).

Histologic and immunohistologic bone marrow examination

Histologic staining of paraffin-embedded tissue sections of 2 decalcified bone marrow biopsy specimens was performed, as previously described.[25] Immunohistologic staining was done with a panel of antibodies against CD10, CD22, CD3, and CD5 from Novocastra (Newcastle upon Tyne, United Kingdom); CD19, CD20, CD117, CD79a, paired box 5 (PAX-5), and terminal deoxynucleotidyl transferase (TdT) from DAKO (Glostrup, Denmark); and CD71, CD34, CD61, CD14, and tryptase from Cell Marque (Rocklin, Calif) on an automated Leica BOND III immunohistological stainer (Leica, Wetzlar, Germany). Total bone marrow cellularity and representation of individual lineages were estimated by comparing the individual cellular compartments with age-matched control tissue.

Neutrophil migration

Ninety-six-well transwell plates containing a 5-μm pore size membrane (Corning, Corning, NY) were used to assess cell migration toward chemoattractants. Freshly isolated neutrophils (5×10^4 cells in 50 μL) were loaded on the top of the transwell filter, and 150 μL of fMLP was added at the indicated concentrations to the lower chamber. After 30 minutes
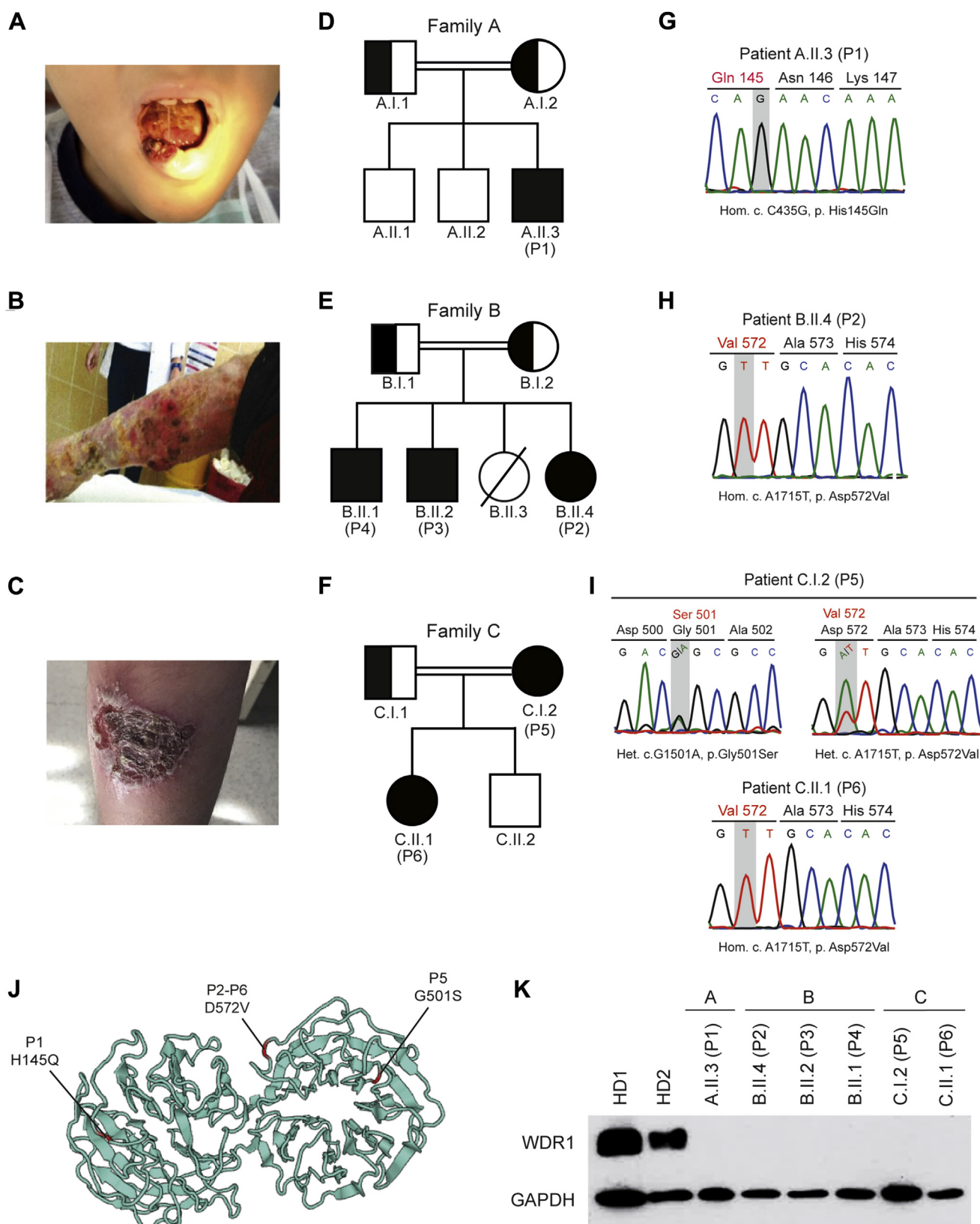
FIG 1. Identification of novel *WDR1* mutations in 3 kindreds. **A,** Aphthous stomatitis in patient P1. **B,** Skin infection on the calf of patient P3. **C,** Skin ulceration on the calf of patient P5. **D,** Pedigree of family A. **E,** Pedigree of family B. **F,** Pedigree of family C. **G,** Sanger validation of *WDR1* mutation in patient P1 (c.C435G, p.His145Gln). **H,** Sanger validation of *WDR1* mutation in patient P2 (c.A1715T, p.Asp572Val). **I,** Sanger validation of the compound heterozygous variants in patient P5 (c.A1715T, p.Asp572Val and c.G1501A, p.Gly501Ser) and homozygous variant in patient P6 (c.A1715T, p.Asp572Val). **J,** Three-dimensional structure of WDR1 with localization of the identified variants. **K,** Representative Western blot analysis of WDR1 expression in lysates from PBMCs isolated from 2 healthy donors and the 6 patients. Glyceraldehyde-3-phosphate dehydrogenase *(GAPDH)* is shown as the loading control. The data correspond to 1 experiment of 2 performed. *HD,* Healthy donor.

TABLE I. Clinical characteristics of the patients

Family	A	B			C	
Patient	1	2	3	4	5	6
Sex	Male	Female	Male	Male	Female	Female
Ethnic origin	Turkish	Turkish	Turkish	Turkish	Syrian	Syrian
Current age (y)	11	12	21	24	26	7
Age at onset (y)	2.5	9	11	14	NA	NA
Consanguinity	Yes	Yes	Yes	Yes	No	Yes
Clinical presentation						
General	Recurrent fever (4- to 6-mo intervals) No dysmorphy obvious facial Diarrhea and vomiting Weight and height: 27 kg (0 SDS, 50th-75th percentile) and 128 cm (0.2 SDS, 50th-75th percentile) at time of admission (8 y)	No recurrent fever Facial dysmorphy (frontal bossing, minimal hypertelorism, wide nasal nostrils) No gastrointestinal manifestations Weight and height: 16.7 kg (−3.9 SDS, <3rd percentile) and 112 cm (−3.6 SDS, <3rd percentile)	No recurrent fever Facial dysmorphy (frontal bossing, minimal hypertelorism, wide nasal nostrils) Diarrhea Weight and height: 43 kg [−3.8 SDS, <3rd percentile] and 162 cm (−2 SDS, <3rd percentile)	No recurrent fever Facial dysmorphy (frontal bossing, minimal hypertelorism, wide nasal nostrils) Diarrhea Weight and height: 50 kg (−2.5 SDS, <3rd percentile) and 168 cm (−1.2 SDS, 10th-25th percentile)	No recurrent fever No obvious facial dysmorphism No gastrointestinal manifestations Weight and height: 75 kg (+1.2 SDS, 90th percentile) and 160 cm (−0.5 SDS, 25th-50th percentile)	Recurrent fever (1-to 2-mo intervals) No obvious facial dysmorphy No gastrointestinal manifestations Weight and height: 20 kg (25th percentile) and 116 cm (10th-25th percentile)
Neurological	Mental impairment (WISC-R test; Verbal IQ: 72, Performance IQ: 84 Total IQ: 75)	Learning difficulty in school, no formal test performed	Learning difficulty in school, no formal test performed	Learning difficulty in school, no formal test performed	Learning difficulty in school, no formal test performed	Learning difficulty in school, no formal test performed
Infections	Pneumonia Aphthous stomatitis Oral candidiasis	Pneumonia Bronchiectasia Aphthous stomatitis Otitis Encephalitis (suspected from viral infection; responsible agent not isolated) Lymphadenopathy Abscesses Varicella infection *Burkholderia gladioli* isolated from skin abscess	Pneumonia Bronchiectasia Nodulocystic acne Skin ulcers Pyoderma gangrenosum HBV carrier *Staphylococcus aureus* infection	Bronchitis Bronchiectasia Nodulocystic acne Abscesses Skin ulcers Lymphadenopathy Pyoderma gangrenosum HBV carrier *Staphylococcus aureus* infection	Aphthous stomatitis Otitis media Sinusitis Pharyngitis Abscesses	Pneumonia Aphthous stomatitis Vesicular lesion Subcorneal pustular dermatosis
Autoinflammation and autoimmunity	Autoimmune thyroiditis Chronic thrombocytopenia Noninflammatory myopathy		Fluctuating thrombocytopenia	Splenomegaly Fluctuating thrombocytopenia		
Treatment	IVIG Fluconazole and trimethoprim-sulfamethoxazole prophylaxis	IVIG Fluconazole and trimethoprim-sulfamethoxazole prophylaxis Inhaler steroid and salbutamol	IVIG Trimethoprim-sulfamethoxazole prophylaxis + Colchicum-Dispert	IVIG Trimethoprim-sulfamethoxazole prophylaxis + Colchicum-Dispert	None	IVIG Fluconazole and trimethoprim-sulfamethoxazole prophylaxis

IVIG, Intravenous immunoglobulin replacement; *NA*, not available/applicable; *SDS*, Standard deviation score; *WISC-R*, Wechsler Intelligence Scale for Children–Revised.

TABLE II. Immunologic characterization of the patients

Family	A				B			
Patient	1				2			3
Age at evaluation (y)	7	8	9	11	9	11	12	18
Hemoglobin (g/dl)	11	10.6	12.2	10.3	9.5	10.3	9	5.83
Lymphocyte count (cells/μL)	2,300 (1,500-7,600)	830 (1,500-7,600)	1,910 (1,500-7,600)	1,920 (1,700-5,700)	3,810 (1,500-7,600)	4,540 (1,700-5,700)	2,630 (1,700-5,700)	3,000 (1,700-5,700)
Neutrophil count (cells/μL)	4,600	18,020	2,200	3,810	16,160	19,370	4,580	10,900
Platelet count (cells/μL)	63,000 (150,000-450,000)	27,000 (150,000-450,000)	55,000 (150,000-450,000)	54,000 (150,000-450,000)	389,000 (150,000-450,000)	440,000 (150,000-450,000)	277,000 (150,000-450,000)	422,000 (150,000-450,000)
MPV (fL)	10.1	10.9	13.7	12.2	8.2	8.3	9.1	8.17
IgG (g/L)	5.72 (without substitution) (4.11-14.35)	3.71 (without substitution) (4.11-14.35)	7.06 (IVIG substitution) (6.54-15.94)	10.40 (IVIG substitution) (6.54-15.94)	13.3 (without substitution) (6.54-15.94)	8.1 (IVIG substitution) (6.54-15.94)	13.6 (IVIG substitution) (6.98-11.94)	11.2 (without substitution) (5.84-14.86)
IgA (g/L)	1.95 (0.34-2.14)	1.09 (0.34-2.14)	0.31 (0.11-2.51)	0.99 (0.11-2.51)	1.57 (0.11-2.51)	1.49 (0.11-2.51)	1.19 (0.22-2.74)	0.98 (0.91-3.93)
IgM (g/L)	0.72 (0.15-1.15)	0.29 (0.15-1.15)	0.27 (0.13-1.45)	0.53 (0.13-1.45)	0.26 (0.13-1.45)	0.34 (0.13-1.45)	0.39 (0.19-0.99)	0.37 (0.32-2.23)
Response to vaccination antigens	Anti-rubella: 52 IU/mL (positive, N: >10 IU/mL) Anti-tetanus: 5 IU/mL (positive, N: >0.1 IU/mL) Anti-diphtheria: 1.61 IU/mL (positive, N: >1 IU/mL) Anti-HBsAg: <5 mIU/mL (negative, N: >10 mIU/mL)				Anti-tetanus <0.1 IU/mL (negative, N: >0.1 IU/mL) Anti-HBsAg: 5 mIU/mL (negative, N: >10 mIU/mL)			
CD19+ B cells (cells/μL)	NA	100 (200-2,200)	170 (200-2,200)	190 (200-1,400)	60 (200-2,200)	164 (200-1,400)	112 (200-1,400)	5 (200-1,400)
CD3+ T cells (cells/μL)	NA	570 (1,000-4,900)	1,490 (1,000-4,900)	1,474 (1,100-4,100)	3,090 (1,000-4,900)	2,670 (1,100-4,100)	3,196 (1,100-4,100)	1,743 (1,100-4,100)
CD4+ T cells (cells/μL)	NA	340 (500-2,700)	760 (500-2,700)	705 (600-2,400)	1,780 (500-2,700)	1,596 (600-2,400)	1,838 (600-2,400)	976 (600-2,400)
CD8+ T cells (cells/μL)	NA	240 (300-2,100)	650 (300-2,100)	648 (400-1,500)	1,220 (300-2,100)	981 (400-1,500)	1,226 (400-1,500)	744 (400-1,500)
NK cells (cells/μL)	NA	120 (200-900)	220 (200-900)	223 (200-1,000)	290 (200-900)	337 (200-1,000)	595 (200-1,000)	302 (200-1,000)
Neutrophil function (BURST test)	Normal				NA			Normal
Other	Anti-thyroglobulin and anti-TPO autoantibodies: positive Cranial MRI: normal				Parahormone and growth hormone stimulation tests: normal			

Normal ranges are shown in parentheses. Normal range for cell types in children is according to Ikinciogullari et al,[29] normal range for cell types in adults is according to Coman-Bitter et al,[30] normal range for immunoglobulins in children is according to Stiehm and Fudenberg,[31] and normal range for immunoglobulins in adults is according to Puissant-Lubrano et al.[32]

IVIG, Intravenous immunoglobulin replacement; *MPV*, mean platelet volume; *MRI*, magnetic resonance imaging; *NA*, not available/applicable; *NK*, natural killer; *TPO*, thyroperoxidase.

of incubation at 37°C, transmigrating cells were collected, transferred into a U-bottom 96-well plate, and counted with a Fortessa flow cytometer (BD Biosciences). The proportion of migrating cells was normalized to the initial input cell number.

Expansion of T and B cells

Patient and healthy donor T cells were expanded by using a feeder cell mixture, as previously described,[26] and maintained in RPMI 1640 medium containing L-glutamine (Gibco, Life Technologies, Grand Island, NY) supplemented with 1% penicillin/streptomycin (Invitrogen, Carlsbad, Calif) and 10% heat-inactivated human serum (all from Gibco). Culturing conditions were 37°C in a humidified 5% CO_2 atmosphere. EBV-immortalized B-lymphoblastic cell lines (B-LCLs) were generated by adding EBV viral supernatant onto freshly isolated PBMCs. The following day, 1 μg/mL

cyclosporin A was added to the cells, which were cultured in RPMI 1640 medium with L-glutamine supplemented with 1% penicillin/streptomycin (Invitrogen) and 10% heat-inactivated FCS (Gibco, Life Technologies).

Morphology and apoptosis of B-LCLs

The morphology and F-actin content of B-LCLs was assessed on combined B-cell receptor (BCR)/Toll-like receptor (TLR) stimulation. Eight-well slides (ibidi, Martinsried, Germany) were coated with anti-IgA/IgG/IgM (10 μL/mL; Abcam, Cambridge, United Kingdom) overnight at 4°C. After washing, cells were seeded in the presence of 5 μmol/L CpG ODN 2006 (InvivoGen, San Diego, Calif) and 1 μmol/L SiR-Actin (Tebu-bio, Le Perray-en-Yvelines, France). After 3 hours, bright-field, total internal reflection fluorescence (TIRF), and interference reflection microscopy (IRM) images of live cells were acquired with a Nikon inverted spinning disk confocal

TABLE II. *(Continued)*

B					C			
3		4			5	6		
20	21	21	23	23	26	5	6	7
12	13.7	10.5	12.5	14	NA	9.6	NA	9.1
2,480 (1,600-2,500)	2,780 (1,600-2,500)	1,170 (1,600-2,500)	1,400 (1,600-2,500)	1,180 (1,600-2,500)	1,500 (1,900-2,800)	1,360 (1,500-5,200)	NA	1,600 (1,500-7,600)
9,310	29,700	8,000	7,600	2,110	8,770	11,670	NA	14,830
108,000 (150,000-450,000)	125,000 (150,000-450,000)	120,000 (150,000-450,000)	105,000 (150,000-450,000)	49,000 (150,000-450,000)	174,000 (150,000-450,000)	213,000 (150,000-450,000)	NA	191,000 (150,000-450,000)
10.2	9.79	9.6	8.32	9.03	9.2	8.8	NA	9.2
10.3 (IVIG substitution) (5.84-14.86)	8.5 (IVIG substitution) (5.84-14.86)	6.96 (without substitution) (5.84-14.86)	10.0 (IVIG substitution) (5.84-14.86)	9.27 (IVIG substitution) (5.84-14.86)	15.3 (without substitution) (5.84-14.86)	5.45 (without substitution) (4.73-13.85)	NA	9.65 (without substitution) (4.11-14.35)
0.97 (0.91-3.93)	0.69 (0.91-3.93)	2.18 (0.91-3.93)	2.18 (0.91-3.93)	2.01 (0.91-3.93)	2.50 (0.91-3.93)	6.25 (0.39-1.47)	NA	9.65 (0.34-2.14)
0.33 (0.32-2.23)	0.24 (0.32-2.23)	0.23 (0.32-2.23)	0.42 (0.32-2.23)	0.36 (0.32-2.23)	2.20 (0.50-2.60)	0.53 (0.20-0.92)	NA	0.37 (0.15-1.15)
Anti-tetanus: 0.15 IU/mL (positive, N: >0.1 IU/mL) Anti-pneumococcus: 4 mg/L (positive, N: >1.3 mg/L)		Anti-tetanus: 0.5 IU/mL (positive, N: >0.1) Anti-pneumococcus: 16 mg/L (positive, N: >1.3 mg/L)			NA	Anti-tetanus: >5 IU/mL (positive, N: >0.1 IU/mL) Anti-rubella: 15 IU/mL (Positive, N: 10-15 IU/mL) Anti-HBsAg: 45 mIU/mL (positive, N: >10 mIU/mL)		
25 (130-260)	28 (130-260)	7 (130-260)	14 (130-260)	12 (130-260)	41 (170-270)	53 (300-1,200)	89 (200-2,200)	60 (200-2,200)
1,959 (700-2,100)	2,113 (700-2,100)	506 (700-2,100)	882 (700-2,100)	732 (700-2,100)	1,351 (700-2,100)	1,168 (1,900-3,600)	1,355 (1,000-4,900)	1,194 (1,000-4,900)
967 (300-1,400)	1,029 (300-1,400)	312 (300-1,400)	588 (300-1,400)	484 (300-1,400)	576 (300-1,400)	582 (600-2,000)	648 (500-2,700)	511 (500-2,700)
794 (200-900)	945 (200-900)	213 (200-900)	364 (200-900)	295 (200-900)	699 (200-900)	560 (300-1,300)	633 (300-2,100)	581 (300-2,100)
99 (90-600)	278 (90-600)	77 (90-600)	224 (90-600)	260 (90-600)	72 (90-600)	119 (200-1,200)	159 (200-900)	200 (200-900)
Normal					NA	Normal		

microscope (Nikon, Tokyo, Japan) equipped with a back-thinned charge-coupled device camera (Evolve, 512 × 512 pixels; Photometrics, Tucson, Ariz), a temperature- and CO_2-controlled chamber, and an oil immersion ×100/1.49 NA objective. The morphologic parameters of the acquired cells were quantified with ImageJ software, applying masks to the bright-field images. Apoptosis of B-LCLs was measured on stimulation with 1.5 μL/mL anti-IgA/IgG/IgM and 5 μmol/L CpG ODN 2006. At the indicated time points, cells were stained on ice with Annexin V–APC (3 μL per 100 μL; BD Biosciences) and propidium iodide (1.5 μL per 100 μL; BioLegend, San Diego, Calif) in Annexin V binding buffer (eBioscience) for 5 minutes, topped up with an additional 200 μL of binding buffer, and kept on ice for acquiring by using flow cytometry. Gates were defined by means of comparison with apoptotic control samples treated at 65°C for 10 minutes.

B-cell somatic hypermutation and class-switch recombination

PBMCs were collected for patients and healthy donors, as described above. RNA extraction was carried out according to the RNeasy Kit protocol (Qiagen, Hilden, Germany). Elution was done twice with 25 μL of RNase-free water. Two independent multiplex PCR reactions were performed by using VH1-6 FR1 forward primers and IGHA or IGHG reverse primers, respectively. The obtained PCR fragments were cloned into pGEM-t Easy Vector (Promega, Madison, Wis), and sequencing of single clones was performed on an ABI Prism 3130XL (Applied Biosystems, Foster City, Calif). After demultiplexing the raw data, FASTA files were uploaded into the IMGT High-V-Quest database, and the resulting files were analyzed by using the

somatic hypermutation (SHM) and class-switch recombination pipeline in ARGalaxy. The clonality of the complementarity-determining region (CDR) 1–CDR3 region was analyzed by using Change-O. SHM analysis was done, as previously described.[27]

Calcium flux experiments on supported lipid bilayers

Calcium flux was assessed in expanded T cells confronted with stimulatory glass-supported lipid bilayers (SLBs), as described previously,[21] with the modifications described below. Briefly, T cells (0.5-1 × 10^{6}) were loaded with 5 μmol/L Fura-2 AM (Invitrogen) in complete RPMI 1640 medium for 30 minutes at 25°C and then washed twice with 10 mL of imaging buffer (1× HBSS [Gibco] supplemented with 1% FCS [Sigma, St Louis, Mo], 1 mmol/L MgCl$_2$ and 1 mmol/L CaCl$_2$). For imaging, cells were spotted onto SLBs functionalized with OKT3-derived single-chain variable fragments at indicated densities and intercellular adhesion molecule 1 (ICAM-1; 50 ng/well or approximately 100 ng/mL). SLB protein density determination was performed, as previously described.[28] Image acquisition was performed with a DMI4000B microscope (Leica Microsystems) equipped with a ×20 objective (Leica ×20 PH2) and an Andor iXon Ultra-8871 EM-CCD camera (Andor Technology, Belfast, United Kingdom) controlled by Metamorph Imaging software (Molecular Devices, Eugene, Ore). Imaging of Fura-2 (excitation, 340 nm and 380 nm; emission, 510 nm) was achieved with the use of a fast external excitation filter wheel equipped with band pass filters at 340 and 380 nm (Leica Fura EX) and a filter cube consisting an emission band pass filter at 520 nm (Fura-2 Leica EM520/36, DC:409). Fura-2 images were collected at intervals of 30 seconds over approximately 10 minutes. Intracellular calcium dynamics were determined ratiometrically from Fura-2 emissions acquired through 340 and 380 nm of excitation by using the open-source Fiji software package. Ratios of Fura-2 emissions were normalized with regard to the first acquired Fura-2 emission ratio determined for nonactivated T cells, which had not yet established productive contacts with the SLB. T cells contacting SLBs featuring ICAM-1 alone were recorded for each healthy donor and patient and served as negative controls.

Statistical analysis

Statistical analyses were performed with GraphPad software. Statistical significance was determined by performing 2-tailed nonparametric t tests. Resulting P values are indicated as follows: ns, $P > .05$, *.01 $< P < .05$, **.001 $< P < .01$, and ***$P < .001$.

RESULTS
Clinical characteristics of the patients

Here we studied 6 patients from 3 consanguineous pedigrees experiencing skin ulcerations, multiple respiratory tract and other infections, intellectual impairment, and in 3 cases stomatitis inflammation (Fig 1, A-F, and Tables I and II).[29-32] A detailed case report is provided in a separate document (see the Methods section and Tables E1 and E2 in this article's Online Repository at www.jacionline.org).

Identification of novel *WDR1* gene mutations in 3 families, resulting in reduced WDR1 expression

Given the consanguineous background of the 3 families, the shared phenotypic traits within the patients, and the absence of clinical signs of immunodeficiency in the unaffected siblings and parents (with the exception of family C), we suspected a common autosomal recessive disease trait. We performed whole-exome sequencing to identify the underlying genetic disease cause. Patient P1 (family A) was found to carry a homozygous missense variant on chromosome 4, 10099458: G>C (hg19 build 137; NM_017491.3: c.C435G, p.His145Gln) in *WDR1* (Fig 1, G).

Patient P2 (family B), as well as patients P3 and P4, were found to carry a homozygous missense variant (c.A1715T, p.Asp572Val) in *WDR1* (Fig 1, H). Patient P6 (family C) was found to carry the same mutation as identified in family B (c.A1715T, p.Asp572Val), and patient P5, the mother of P6, was found to be a heterozygous carrier of the p.Asp572Val mutation together with another heterozygous variant (c.G1501A, p.Gly501Ser; Fig 1, I). These *WDR1* gene variants have not been observed in heterozygous or homozygous form in several human genetic variation databases, including the 1000 Genomes Project and the Exome Aggregation Consortium. In addition, the heterozygous carriers did not show any symptoms. The variant found in family A (H145Q) was predicted to be benign and tolerated, with a CADD score of 13.3. The variant identified in families B and C (D572V) was predicted to be damaging and deleterious based on PolyPhen-2 and SIFT predictors for the corresponding protein function, with a CADD score of 28. The heterozygous variant identified in patient P5 (G501S) was predicted to be damaging and deleterious, with a CADD score of 26.7.

The *WDR1* gene variants found in the 3 families segregated perfectly with the disease under the assumption of autosomal recessive inheritance (see Fig E1 in this article's Online Repository at www.jacionline.org). Although variants in additional genes also segregated within the individual families (see Table E3 in this article's Online Repository at www.jacionline.org), they were disregarded as being causative because they could not be related to the immunodeficiency status of the patients. Additionally, the striking similarities between the clinical phenotypes in the 3 families pointed to the *WDR1* variants as the common cause of the immunopathology. The 3 identified mutations are located in coils between antiparallel β-sheet repeats, which might affect the 3-dimensional blade structure of WDR1 and its overall stability (Fig 1, J).

We analyzed WDR1 expression in the patients' PBMCs by using Western blotting. The newly identified mutations were associated with near-absent levels of WDR1 expression (Fig 1, K). However, we observed variable residual WDR1 expression in both expanded T cells from the patients, suggesting that lymphocyte activation might stimulate or stabilize expression of the WDR1 variants (see Fig E2, A, in this article's Online Repository at www.jacionline.org).

Together, our data demonstrate that the newly identified *WDR1* mutations lead to a marked WDR1 expression defect in peripheral blood cells from the patients, reinforcing the link of causality between the *WDR1* mutations and the immunopathology affecting the patients.

Neutrophil and monocyte defects associated with *WDR1* mutations

On blood smear examination, we detected abnormal herniation of neutrophil nuclear lobes (data not shown). This characteristic observation is in line with the recent identification of *WDR1* mutations in immunodeficient patients for whom neutrophil nuclear herniation and associated defects were identified as a hallmark of the disease.[4] Neutrophils were purified and stained with Phalloidin and 4′-6-diamidino-2-phenylindole dihydrochloride to further characterize the morphologic defects associated with mutant WDR1. Approximately half of the neutrophils from the patients with *WDR1* mutations had aberrant morphology (Fig 2,
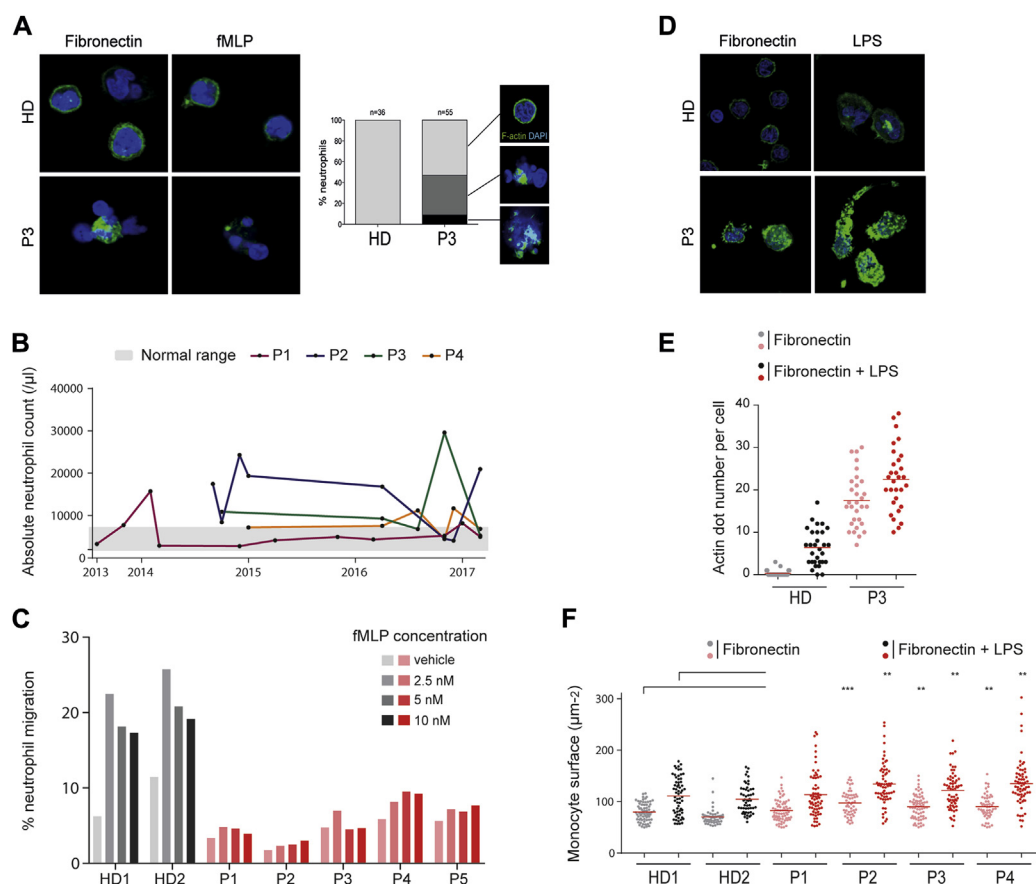
FIG 2. Effect of *WDR1* variants on neutrophils and monocytes. **A,** Representative picture of neutrophils from a healthy donor and patient P3 deposited on fibronectin or fibronectin plus fMLP. Morphologies of fMLP-stimulated neutrophils (36 from a healthy donor and 55 from patient 3) classified as normal *(light gray)*, nuclear herniations *(dark gray)*, or complex aberrations *(black)*. **B,** Five-year longitudinal analysis of neutrophil absolute counts in patients P1 to P4. The normal range is indicated in gray. **C,** Migration of neutrophils from 2 healthy donors and patients P1 to P5 in response to indicated concentrations of fMLP. Data correspond to 1 experiment of 2 performed. **D,** Representative picture of monocytes from a healthy donor and patient P3 on spreading over fibronectin or fibronectin plus LPS. **E,** Number of actin dots quantified in 30 monocytes from a healthy donor and patient P3. Data correspond to 1 experiment of 2 performed. **F,** The surface covered by monocytes spreading over fibronectin *(gray and light red dots)* or fibronectin plus LPS *(black and red dots)* was quantified in 60 monocytes from 2 healthy donors and patients P1 to P4. Data pertaining to morphologic aberrations in neutrophils were confirmed in independent experiments performed on a second blood sampling from patients P1 to P4. *HD,* Healthy donor. ******.001 < *P* < .01, and ********P* < .001.

A). They displayed either nuclear herniation with 1 or more nuclear lobes protruding from the cell body or a loss of nuclear integrity, as revealed by spread 4′-6-diamidino-2-phenylindole dihydrochloride staining. These morphologic aberrations were associated with dissolution of cortical actin and abnormal accumulation of filamentous actin toward the cell center, as determined based on F-actin staining. Therefore our immunofluorescence data suggest that loss-of-function mutations in *WDR1* affect actin turnover, thereby leading to both a weakening of the cell cortex and accumulation of cytoplasmic actin structures. This process either pushes nuclear lobes out of the cell body or more profoundly disrupts nuclear integrity. These morphologic defects were not associated with reduced numbers of circulating neutrophils. On the contrary, patients had normal to increased neutrophil counts in peripheral blood (Fig 2, *B*). We further explored how such morphologic aberration might affect the capacity of neutrophils to survive and migrate.

Neutrophils from the patients with *WDR1* mutations did not consistently display accelerated loss of mitochondrial membrane potential (see Fig E3, *A*, in this article's Online Repository at www.jacionline.org) or increased apoptosis (see Fig E3, *B* and *C*). However, a transwell assay revealed impaired migration of neutrophils from the patients with *WDR1* mutations in response to fMLP (Fig 2, *C*). Therefore our data reinforce the notion that biallelic *WDR1* mutations in human subjects are associated with a characteristic phenomenon of neutrophil herniation, with defective migration toward fMLP.

We next investigated whether morphologic aberrations would apply to monocytes. On blood isolation and seeding over fibronectin-coated slides, monocytes from the patients with *WDR1* mutations emitted actin dots oriented toward the substrate, which were not detectable in normal monocytes (Fig 2, *D*). These structures are reminiscent of actin-rich podosomes, which are assembled in macrophages and monocyte-derived dendritic
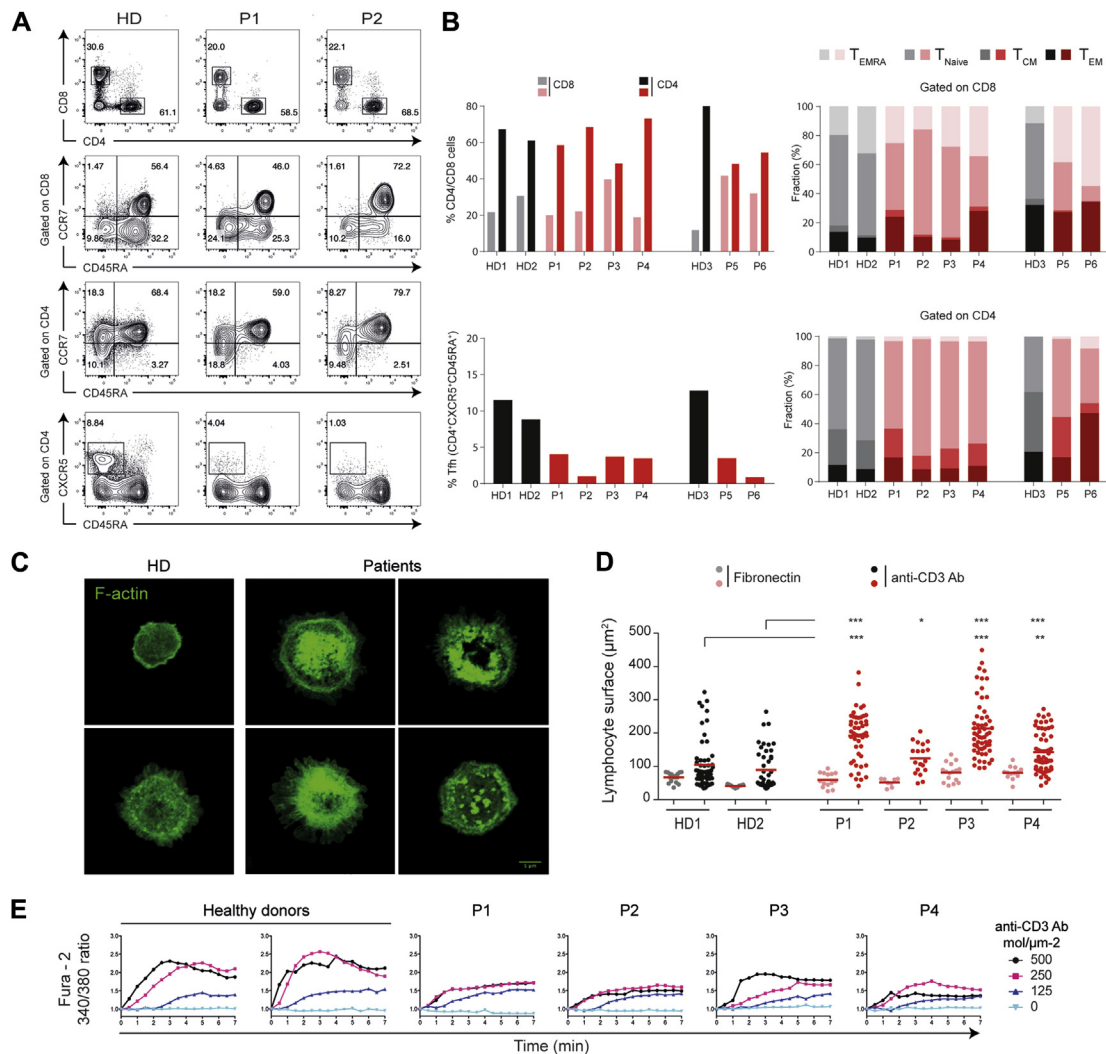
FIG 3. Effect of *WDR1* variants on T-cell activation and function. **A,** Representative flow cytometric analysis of T-cell subsets in PBMCs from a healthy donor and patients P1 and P2. **B,** Flow cytometry–based quantification of the indicated T-cell subsets in PBMCs from 3 healthy donors and the 6 patients. Data correspond to 1 experiment of 2 performed for patients P5 and P6 and of 1 experiment for patients P1 to P4. **C,** Representative images of F-actin staining in primary T cells from a healthy donor and patients P2 *(upper panels)* and P3 *(lower panels)* spreading over coated anti-CD3 antibody. Comparable morphologic aberrations were observed in an experiment performed on a second blood sampling from patients P1 to P4. **D,** T-cell surface on spreading over fibronectin (gray and light red dots) or anti-CD3 antibody (black and red dots) in 2 healthy donors and patients P1 to P4. Ten to 60 T cells were analyzed per condition. Data correspond to 1 experiment of 2 performed. **E,** Calcium influx in expanded T cells from 2 healthy donors and patients P1 to P4 stimulated over a lipid bilayer presenting ICAM-1 and anti-CD3 antibodies. Data correspond to 1 experiment of 2 performed. *HD,* Healthy donor. *.01 < P < .05, **.001 < P < .01, and ***P < .001.

cells.[33] Similar structures were observed in normal monocytes on LPS stimulation. Evidently, patients' monocytes emitted a significantly higher number of actin dots when compared with control monocytes on LPS stimulation (Fig 2, *E*). These observations are in agreement with previous findings of increased podosome assembly in dendritic cells from patients with *WDR1* mutations.[5] In parallel, we measured an increased ability of patients' monocytes to spread over fibronectin spontaneously or on LPS stimulation (Fig 2, *F*). In conclusion, monocytes isolated from the blood of patients with *WDR1* mutations displayed increased basal and LPS-driven spreading associated with podosome-like F-actin structures.

TCR activation in *WDR1*-mutated T lymphocytes

In view of the pleiotropic expression of WDR1, we reasoned that *WDR1* mutations might also affect functional integrity of lymphoid cells. We first investigated the T-cell compartment of patients through phenotypic characterization of peripheral blood T-cell subsets. Although normal proportions of T cells belonging to the CD4^{+}, CD8^{+}, naive, central memory, effector memory, and stem memory subsets were detected, follicular helper T (Tfh) cells were present in a reduced proportion in all 6 patients (Fig 3, *A* and *B*, and see Fig E2, *B*). We then investigated actin cytoskeletal organization in T cells from patients P1 to P4 on interaction with anti-CD3 antibody–coated slides. Somewhat
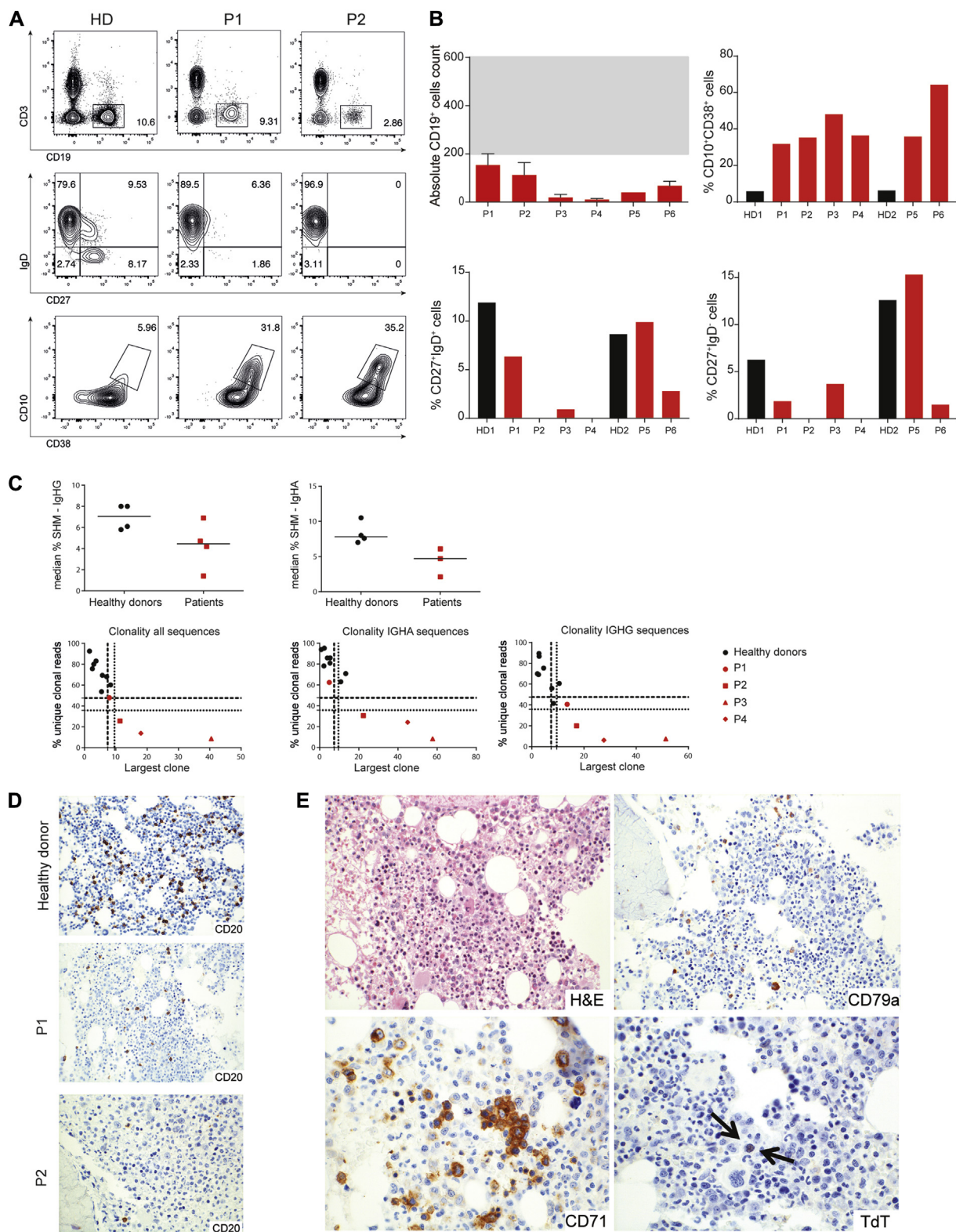
FIG 4. Effect of *WDR1* variants on the B-cell compartment. **A,** Representative flow cytometric analysis of B-cell subsets in PBMCs from a representative healthy donor and patients P1 and P2. **B,** Absolute numbers of peripheral B cells (*upper left panel*, mean ± SD of 3 values, normal range in gray) and proportion of CD19$^+$ B-cell subsets from 2 healthy donors and the 6 patients: transitional B cells (CD10$^+$CD38$^+$, *upper right panel*), IgM/D memory B cells (CD27$^+$IgD$^+$, *lower left panel*), and IgG memory B cells (CD27$^+$IgD$^-$, *lower right panel*). Data correspond to 1 experiment of 2 performed for patients P5 and P6 and of 1 experiment for patients P1 to P4. **C,** Analysis of B-cell clonal diversity in PBMCs from 8 healthy donors and patients P1 to P4. Clonal diversity is represented as plots depicting the relative size of the largest clone and the proportion of unique clonal reads for all sequences, IgA sequences, and IgG sequences (*upper plots*). SHM events in B cells from healthy donors and patients P1 to P4 (*lower plots*). **D,** Immunohistology of bone marrow from an age-matched healthy donor and patients P1 and P2. **E,** Immunohistologic staining for hematoxylin and eosin (*H&E*), CD71, CD79a, or terminal deoxynucleotidyl transferase (*TdT*) in bone marrow from patient P1. *HD,* Healthy donor.

reminiscent of what we observed in the monocytes, the tested T cells from patients displayed aberrant actin meshwork organization and increased spreading (Fig 3, *C* and *D*). The abnormal actin structures identified in *WDR1*-mutant lymphocytes included actin arcs, actin spikes, and filopodia, which were described to be dependent on formin activity.[34] This suggests that the defect in actin turnover associated with WDR1 deficiency results in increased assembly of structures that might depend on formin rather than Arp2/3 activity.

We then tested which aspects of TCR-mediated activation might be controlled by WDR1. T cells derived from all tested patients (P1-P4) displayed a diminished calcium response, which was reduced in amplitude at intermediate and high densities of stimulatory anti-CD3 antibodies (Fig 3, *E*). This indicates a role for WDR1 in tuning TCR-proximal signaling. Differently, the later event of TCR internalization was not affected in *WDR1* mutant T cells from patients P1 to P4 (see Fig E2, *C*). A recent study reported a defect in anti-CD3 antibody–evoked T-cell proliferation in a patient carrying a *WDR1* mutation.[5] Our analysis of T-cell proliferation from peripheral blood collected at different time points showed inconsistent anti-CD3 antibody–evoked proliferation rates, varying from reduced to normal values (see Fig E2, *D*). In addition, the *WDR1* mutations affected neither the ability of T cells expanded from the blood of patients P1 to P4 to migrate in response to CXCL12 (see Fig E2, *E*) nor the capacity of purified CD8^{+} T cells to kill target cells (see Fig E2, *F*). Together, our data suggest that WDR1 deficiency only mildly affects the development and TCR activation of T lymphocytes.

Abnormal B-cell development in patients with *WDR1* mutations

Although *WDR1* mutations had only a limited effect on production of mature T cells in the periphery, we observed a marked phenotype in the B-cell compartment. Indeed, low B-cell counts were detected in the peripheral blood in all patients reported here (Fig 4, *A* and *B*, and see Fig E4, *A*, in this article's Online Repository at www.jacionline.org). Residual peripheral B cells were abnormally skewed toward the transitional B-cell stage in all 6 patients. Except for patient 5, the proportions of IgM nonswitched (CD27^{+}IgD^{+}) and IgG class-switched memory (IgD^{−}CD27^{+}) cells among the B-cell subset were significantly reduced. This phenotype points toward a defect in B-cell development. Indeed, there was a large accumulation of peripheral blood B cells with a CD10^{+}CD38^{+} phenotype, which is consistent with them being transitional B cells (ie, recent bone marrow emigrants; Fig 4, *A* and *B*, and see Fig E4, *A*).

The paucity of memory B cells might reflect a defect during the steps of class-switch recombination or SHM.

To explore this possibility, we sequenced the CDR1-CDR3 region and analyzed the clonality of the *IGHA* or *IGHG* regions. The BCR repertoire of the 4 tested patients with *WDR1* mutations was of a restricted size, with P3 and P4 harboring an extremely clonal repertoire (Fig 4, *C*). These 2 patients are the oldest (21 and 24 years compared with 11 and 12 years for P1 and P2), which might indicate that the size of the BCR repertoire diminished with age. We further detected decreased SHM in B cells from the patients with *WDR1* mutations (Fig 4, *C*). The mechanisms underlying this observation could include CD4^{+} T-cell lymphopenia, especially Tfh cells, impaired T-cell

proliferation, or an intrinsic B-cell defect. However, SHM targeting (AID and Pol η motifs) and repair (transition/transversion mutation at the AT or GC locations) were normal (see Fig E4, *B*). This suggests no defect in the error-prone repair of mismatch repair or base excision repair that is used during SHM. The median CDR3 length was higher, but this is probably not caused by an increase in JH6 (the longest JH gene) or an increase in the number of N-nucleotides, but the number of deletions is lower in the patients (see Fig E4, *C*). The median CDR3 length in the switched memory B cells is higher in patients compared with control subjects, suggesting that selection for B cells with shorter CDR3 length might be impaired. The abnormal peripheral B-cell compartment might originate from an early bone marrow defect. Bone marrow biopsy specimens were available from patients P1 and P2, which allowed us to perform histologic analysis. In both patients the marrow was normocellular, with a usual topographic arrangement of slightly disrupted erythropoietic (Fig 4, *D* and *E*, and see Fig E5, *A* and *B*, in this article's Online Repository at www.jacionline.org) and myeloid precursor cells. Megakaryocytes were regularly distributed and inconspicuous. Only a few lymphocytes were discerned morphologically.

Immunohistologically, most lymphocytes were CD3^{+} T cells with only singular CD20^{+}/CD79a^{+}/PAX-5^{+}/CD22^{+} B cells intermingled. However, the few B cells were mostly mature, given the fact that they were terminal deoxynucleotidyl transferase and CD10 negative. Compared with the frequency of normal B cells in age-matched control bone marrow biopsy specimens, the very low frequency of CD20^{+} cells points to a severe reduction of bone marrow B-cell precursors.

We then reasoned that the paucity of B-cell precursors in the bone marrow and the reduced ability of the B cells that reach the periphery to differentiate and generate a diversified BCR repertoire could result either from intrinsic BCR signaling defects, motility defects affecting tissue localization and homing, or reduced survival. To test these possibilities, we used B-LCLs generated from the few B cells collected from the peripheral blood of the patients. After stimulation with anti-IgA/IgG/IgM and CpG, B cells from patients with *WDR1* mutations displayed increased adhesion, as determined based on the proportion of cells spreading (Fig 5, *A*). Strikingly, the morphology of the patients' B cells spreading over anti-IgA/IgG/IgM and CpG was characterized by an increased emission of multiple thin protrusions. In agreement with the role of WDR1 in actin turnover, examination of the actin cytoskeleton by using TIRF microscopy of cells prestained with SiR-actin revealed an increased density of polymerized actin at the ventral plane of the cells. Accordingly, the cells carrying *WDR1* mutations displayed a very tight adhesion to the substratum, as observed by using IRM. This propensity of the *WDR1*-mutated B cells to spread resulted in a much wider surface and perimeter than control cells and a reduced circularity (Fig 5, *B*).

We then assessed the ability of the B-LCLs from patients with *WDR1* mutations to migrate directionally. When exposed to a CCL19 gradient, the *WDR1*-mutated B cells migrated normally along the gradient, as assessed by using the forward migration index (see Fig E6 in this article's Online Repository at www.jacionline.org). This suggests that the WDR1-related defect of B cells is restricted to the BCR.

We next investigated whether these B cells might be abnormally prone to apoptosis on BCR/TLR stimulation. B-LCLs from patients P2 and P3 displayed spontaneous
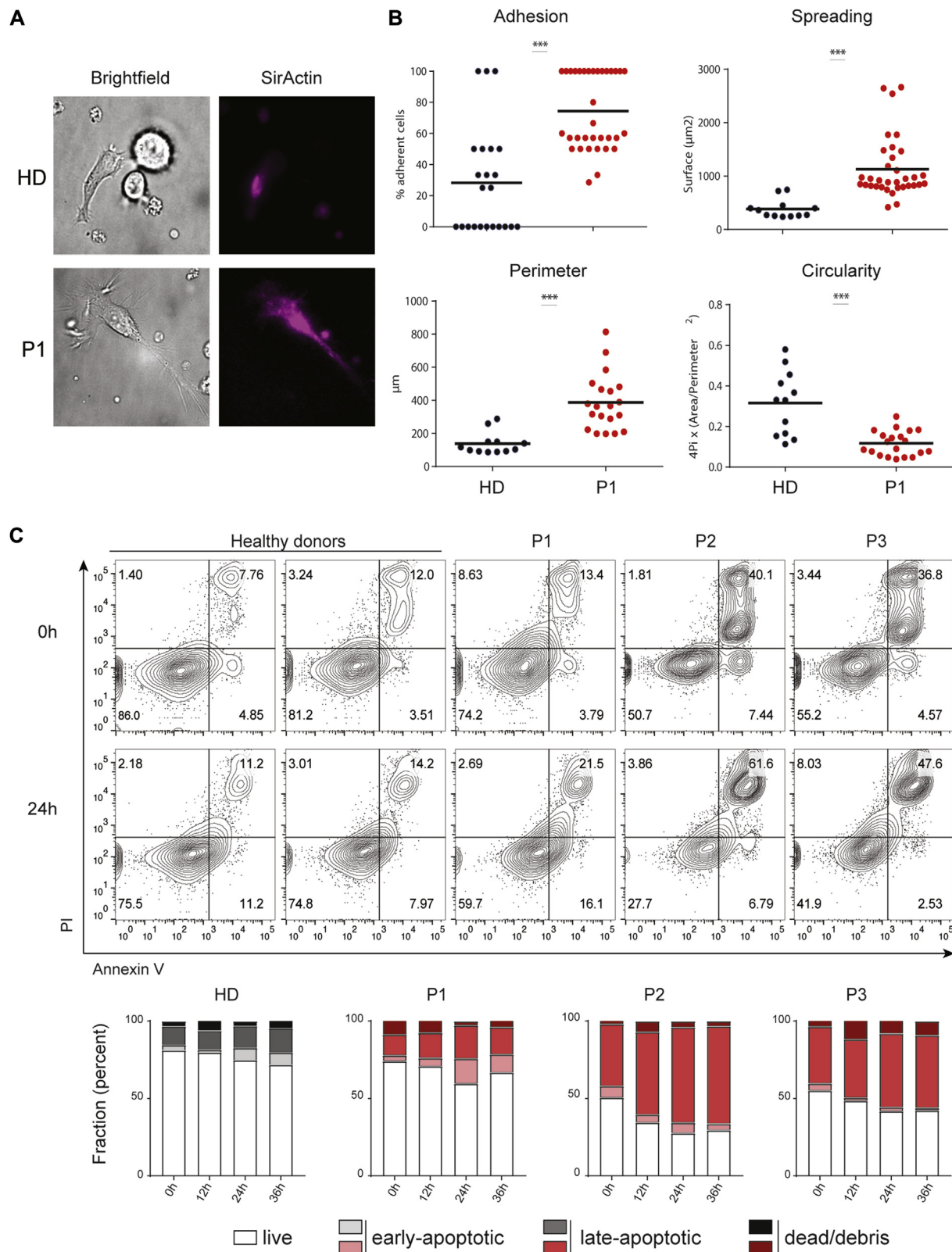
FIG 5. Effect of *WDR1* variants on B-cell activation and apoptosis. **A,** Representative pictures of B-LCLs from a healthy donor and patient P1 on spreading over anti-IgA/IgG/IgM plus CpG. Bright-field and TIRF imaging of F-actin (SiR-Actin) are shown in parallel. The pictures stem from 1 experiment of 2 performed. Data correspond to 1 experiment of 2 performed. **B,** Morphologic parameters of B-LCLs from a healthy donor and patient P1 on spreading over anti-IgA/IgG/IgM plus CpG. **C,** Apoptosis in B-LCLs from 2 healthy donors and patients P1, P2, and P3, as determined by staining for Annexin V and propidium iodide, after 0, 12, 24, or 36 hours of BCR/TLR stimulation. Data correspond to 1 experiment. *HD*, Healthy donor. ***P < .001.

apoptosis, as highlighted by the high proportion of late apoptotic cells (propidium iodide–positive Annexin V[+]) before stimulation (Fig 5, C). The proportion of late apoptotic cells further increased on BCR/TLR stimulation. Although B cells from patient P1 appeared less affected, we noted an increased rate of both early and late apoptotic cells after 24 hours of stimulation.

Collectively, these data highlight the key role of WDR1 in the development and activation of B cells. They further indicate that WDR1 is required for BCR-mediated activation and survival.

DISCUSSION

Here we identified 6 patients from 3 consanguineous families carrying novel *WDR1* biallelic missense mutations leading to defective expression of WDR1 in immune cells. In addition to recently described alteration of myeloid cell morphology and function in the context of WDR1 deficiency,[4,5] our study unravels a previously unappreciated role of WDR1 in lymphocyte activation and development.

The discovery of a number of PIDs caused by deficiency or molecular alteration of actin cytoskeletal remodeling proteins has allowed us to gain insight into the key role of actin cytoskeletal dynamics in supporting immune cell function.[3] In this context the characterization of patients carrying *WDR1* mutations provides a unique insight into a yet poorly studied facet of actin cytoskeletal dynamics in control of leukocyte development, activation, and function.

A hallmark of *WDR1*-mutated leukocytes appears to be the assembly of aberrant actin structures. This applied to T- and B-cell immunologic synapses, as well as to neutrophils and monocytes. Of interest, these structures were specific to each cell subset and were interfering with distinct cellular processes. WDR1-mutated lymphocytes displayed defective activation or survival on antigen receptor triggering, which appeared to be related to abnormal actin turnover at the synapse. Monocytes displayed aberrant spreading in relationship with the assembly of numerous podosome-like structures. Neutrophils appeared to be affected predominantly in their migratory capacity as a probable consequence of the loss of their morphologic integrity. These observations point to a rather selective role of WDR1 in sustaining specific actin-related processes in distinct leukocytes.

The most severe cellular defect identified in our cohort of patients with *WDR1* mutations was a profound B-cell lymphopenia mirrored by low B-cell precursor counts in the bone marrow. In apparent contrast, the few B cells detected in bone marrow were mature B cells, whereas the peripheral B-cell compartment was skewed toward an immature transitional B-cell stage. This might result from a premature release of immature B cells from the bone marrow, as shown in patients with Wiskott-Aldrich syndrome (WAS), another disorder of the actin cytoskeleton.[35] Therefore, for the first time, our study identifies WDR1 as a key actin regulator required for B-cell differentiation. Applying TIRF and IRM microscopy to patient-derived B cell lines, we further observed aberrant activation on BCR/TLR stimulation, leading to multiple actin-rich filopodia associated with elongated B-cell synapse morphology. This is in line with previous studies showing that BCR stimulation depends on actin depolymerization[36] and that cofilin-evoked actin severing is key to BCR-induced synapse formation.[37] The prominent effect of WDR1 deficiency on development of the B-cell compartment might be explained by a role in tonic BCR signaling, a process that depends on actin dynamics and is crucial

for the survival of developing B cells.[38] Indeed, we identified an increased apoptosis rate in B-LCLs derived from patients with *WDR1* mutations on BCR stimulation. We suspect that the B-lymphocyte defects associated with WDR1 deficiency might underlie some of the clinical manifestations, in particular the recurrent infections.

The consequences of the identified *WDR1* mutations on generation of the T-cell compartment appeared less prominent than on generation of the B-cell compartment. Thus, with the exception of Tfh cells, normal proportions of the main T-cell subsets were present in the peripheral blood of the patients from our cohort. The selective reduction in numbers of Tfh cells is likely a consequence of the B-cell deficiency because Tfh cells require B cells for their differentiation and survival.[39] On stimulation with immobilized anti-CD3 antibodies, mature T cells from the patients displayed increased spreading and aberrant actin-rich structures that most probably result from a defect in actin turnover. Such a defect might affect predominantly Arp2/3-driven actin branching and lamellipodia assembly by limiting the availability of actin monomers and capped actin oligomers. In contrast, formin-driven actin filament elongation might be affected to a lesser extent, and its activity would become dominant over that of Arp2/3.

In agreement with this hypothesis, we observed aberrant assembly of long actin filaments, either organized radially and pointing outward or organized as arcs forming a circular belt around the synapse. In agreement with those observations, activation of patients' T cells over a membrane bilayer presenting recombinant ICAM-1 and anti-CD3 antibodies resulted in reduced calcium influx. However, WDR1 deficiency was not consistently associated with reduced anti-CD3–evoked T-cell proliferation, pointing to a rather mild role in TCR-driven activation compared with other PID-associated actin regulators, such as Wiskott-Aldrich syndrome protein (WASP) or dedicator of cytokinesis 8.[40,41] Coronin 1A–mediated actin depolymerization has been shown to facilitate lytic granule delivery in natural killer cells.[42] In our study, however, the identified *WDR1* mutations did not appear to cause a defect in T cell–mediated cytotoxicity in expanded peripheral blood T cells. These observations call for a further exploration of the molecular mechanisms controlling actin depolymerization in the context of the cytotoxic activity of natural killer and CD8^{+} T cells.

Our report expands the phenotypic spectrum of WDR1 deficiency, which comprises marked defects of both innate and adaptive immunity, resulting in severe autoinflammation, predisposition to autoimmunity, and compromised B-cell function. Different from WASP deficiency,[43] the prototypical actin-related PID, thrombocytopenia was inconsistent and platelet volume was normal in patients with *WDR1* mutations. Eczema, a typical manifestation of WAS, was also absent in these patients. However, the recurrent skin infections were reminiscent of those observed in patients with WAS. The characteristic auto-inflammatory manifestations of the patients with *WDR1* mutations are distinct from those of patients with WAS, whereas the autoimmune clinical presentation overlaps between the 2 disease entities. Although this has not been reported yet, it appears likely that WDR1 deficiency is also associated with a greater risk of malignancy, given dysregulated actin polymerization reminiscent of the relatively high risk of myelodysplasia/acute myeloid leukemia in X-linked neutropenia caused by gain-of-function mutations in patients with WAS,[44] and

the impaired immune surveillance for viral and other triggers in general.[45] On that basis, at least for the more severely affected patients, allogeneic hematopoietic stem cell transplantation might be a feasible and rational approach.

Another clinical feature consistently observed in the patients with *WDR1* mutations was mild-to-moderate intellectual disability. Gene variant analysis did not reveal any additional variant that would be shared by the patients presenting with intellectual disability and that might be related to such a clinical presentation. Chronic inflammation or repeated hospitalization periods might have contributed to intellectual disability. Given the pleiotropic expression of WDR1, its deficiency in the central nervous system might also result in neuronal defects. The potential role of WDR1 in neuronal tissues will deserve further investigation in the future.

Key messages

- **Deficiency of the actin regulator WDR1 in human subjects is associated with a paucity of B-cell progenitors in the bone marrow and lack of switched memory B cells in the periphery.**

- ***WDR1* missense mutations lead to aberrant assembly of both T- and B-cell immunologic synapses.**

REFERENCES

1. Blanchoin L, Boujemaa-Paterski R, Sykes C, Plastino J. Actin dynamics, architecture, and mechanics in cell motility. Physiol Rev 2014;94:235-63.
2. Pollard TD. Actin and actin-binding proteins. Cold Spring Harb Perspect Biol 2016;8.
3. Moulding DA, Record J, Malinova D, Thrasher AJ. Actin cytoskeletal defects in immunodeficiency. Immunol Rev 2013;256:282-99.
4. Kuhns DB, Fink DL, Choi U, Sweeney C, Lau K, Priel DL, et al. Cytoskeletal abnormalities and neutrophil dysfunction in WDR1 deficiency. Blood 2016;128: 2135-43.
5. Standing AS, Malinova D, Hong Y, Record J, Moulding D, Blundell MP, et al. Autoinflammatory periodic fever, immunodeficiency, and thrombocytopenia (PFIT) caused by mutation in actin-regulatory gene WDR1. J Exp Med 2017; 214:59-71.
6. Voegtli WC, Madrona AY, Wilson DK. The structure of Aip1p, a WD repeat protein that regulates Cofilin-mediated actin depolymerization. J Biol Chem 2003;278:34373-9.
7. Iida K, Yahara I. Cooperation of two actin-binding proteins, cofilin and Aip1, in Saccharomyces cerevisiae. Genes Cells 1999;4:21-32.
8. Okada K, Obinata T, Abe H. XAIP1: a Xenopus homologue of yeast actin interacting protein 1 (AIP1), which induces disassembly of actin filaments cooperatively with ADF/cofilin family proteins. J Cell Sci 1999;112:1553-65.
9. Rodal AA, Tetreault JW, Lappalainen P, Drubin DG, Amberg DC. Aip1p interacts with cofilin to disassemble actin filaments. J Cell Biol 1999;145:1251-64.
10. Okada K, Blanchoin L, Abe H, Chen H, Pollard TD, Bamburg JR. Xenopus actin-interacting protein 1 (XAip1) enhances cofilin fragmentation of filaments by capping filament ends. J Biol Chem 2002;277:43011-6.
11. Okada K, Ravi H, Smith EM, Goode BL. Aip1 and cofilin promote rapid turnover of yeast actin patches and cables: a coordinated mechanism for severing and capping filaments. Mol Biol Cell 2006;17:2855-68.
12. Ono S. Regulation of actin filament dynamics by actin depolymerizing factor/cofilin and actin-interacting protein 1: new blades for twisted filaments. Biochemistry 2003;42:13363-70.
13. Jansen S, Collins A, Chin SM, Ydenberg CA, Gelles J, Goode BL. Single-molecule imaging of a three-component ordered actin disassembly mechanism. Nat Commun 2015;6:7202.
14. Kueh HY, Charras GT, Mitchison TJ, Brieher WM. Actin disassembly by cofilin, coronin, and Aip1 occurs in bursts and is inhibited by barbed-end cappers. J Cell Biol 2008;182:341-53.
15. Brieher WM, Kueh HY, Ballif BA, Mitchison TJ. Rapid actin monomer-insensitive depolymerization of Listeria actin comet tails by cofilin, coronin, and Aip1. J Cell Biol 2006;175:315-24.
16. Li J, Brieher WM, Scimone ML, Kang SJ, Zhu H, Yin H, et al. Caspase-11 regulates cell migration by promoting Aip1-Cofilin-mediated actin depolymerization. Nat Cell Biol 2007;9:276-86.
17. Kile BT, Panopoulos AD, Stirzaker RA, Hacking DF, Tahtamouni LH, Willson TA, et al. Mutations in the cofilin partner Aip1/Wdr1 cause autoinflammatory disease and macrothrombocytopenia. Blood 2007;110:2371-80.
18. Liu LJ, Zhang XY, He N, Liu K, Shi XG, Feng T, et al. Genetic variation in WDR1 is associated with gout risk and gout-related metabolic indices in the Han Chinese population. Genet Mol Res 2016;15.
19. Qi D, Wu B, Tong D, Pan Y, Chen W. Identification of key transcription factors in caerulein-induced pancreatitis through expression profiling data. Mol Med Rep 2015;12:2570-6.
20. Xu H, Chen Y, Tan C, Xu T, Yan Y, Qin R, et al. High expression of WDR1 in primary glioblastoma is associated with poor prognosis. Am J Transl Res 2016; 8:1253-64.
21. Salzer E, Cagdas D, Hons M, Mace EM, Garncarz W, Petronczki OY, et al. RASGRP1 deficiency causes immunodeficiency with impaired cytoskeletal dynamics. Nat Immunol 2016;17:1352-60.
22. Ozen A, Comrie WA, Ardy RC, Dominguez Conde C, Dalgic B, Beser OF, et al. CD55 deficiency, early-onset protein-losing enteropathy, and thrombosis. N Engl J Med 2017;377:52-61.
23. Kircher M, Witten DM, Jain P, O'Roak BJ, Cooper GM, Shendure J. A general framework for estimating the relative pathogenicity of human genetic variants. Nat Genet 2014;46:310-5.
24. Magi A, Tattini L, Palombo F, Benelli M, Gialluisi A, Giusti B, et al. H3M2: detection of runs of homozygosity from whole-exome sequencing data. Bioinformatics 2014;30:2852-9.
25. Schiefer AI, Kornauth C, Simonitsch-Klupp I, Skrabs C, Masel EK, Streubel B, et al. Impact of single or combined genomic alterations of TP53, MYC, and BCL2 on survival of patients with diffuse large B-cell lymphomas: a retrospective cohort study. Medicine (Baltimore) 2015;94:e2388.
26. Dupre L, Aiuti A, Trifari S, Martino S, Saracco P, Bordignon C, et al. Wiskott-Aldrich syndrome protein regulates lipid raft dynamics during immunological synapse formation. Immunity 2002;17:157-66.
27. de Jong BG, IJspeert H, Marques L, van der Burg M, van Dongen JJ, Loos BG, et al. Human IgG2- and IgG4-expressing memory B cells display enhanced molecular and phenotypic signs of maturity and accumulate with age. Immunol Cell Biol 2017;95:744-52.
28. Axmann M, Schutz GJ, Huppa JB. Single molecule fluorescence microscopy on planar supported bilayers. J Vis Exp 2015;(105):e53158.
29. Ikinciogullari A, Kendirli T, Dogu F, Egin Y, Reisli I, Cin S, et al. Peripheral blood lymphocyte subsets in healthy Turkish children. Turk J Pediatr 2004;46:125-30.
30. Comans-Bitter WM, de Groot R, van den Beemd R, Neijens HJ, Hop WC, Groeneveld K, et al. Immunophenotyping of blood lymphocytes in childhood. Reference values for lymphocyte subpopulations. J Pediatr 1997; 130:388-93.
31. Stiehm ER, Fudenberg HH. Serum levels of immune globulins in health and disease: a survey. Pediatrics 1966;37:715-27.
32. Puissant-Lubrano B, Peres M, Apoil PA, Congy-Jolivet N, Roubinet F, Blancher A. Immunoglobulin IgA, IgD, IgG, IgM and IgG subclass reference values in adults. Clin Chem Lab Med 2015;53:e359-61.
33. Linder S, Aepfelbacher M. Podosomes: adhesion hot-spots of invasive cells. Trends Cell Biol 2003;13:376-85.
34. Murugesan S, Hong J, Yi J, Li D, Beach JR, Shao L, et al. Formin-generated acto-myosin arcs propel T cell receptor microcluster movement at the immune synapse. J Cell Biol 2016;215:383-99.
35. Castiello MC, Bosticardo M, Pala F, Catucci M, Chamberlain N, van Zelm MC, et al. Wiskott-Aldrich Syndrome protein deficiency perturbs the homeostasis of B-cell compartment in humans. J Autoimmun 2014;50:42-50.
36. Hao S, August A. Actin depolymerization transduces the strength of B-cell receptor stimulation. Mol Biol Cell 2005;16:2275-84.
37. Freeman SA, Lei V, Dang-Lawson M, Mizuno K, Roskelley CD, Gold MR. Cofilin-mediated F-actin severing is regulated by the Rap GTPase and controls the cytoskeletal dynamics that drive lymphocyte spreading and BCR microcluster formation. J Immunol 2011;187:5887-900.

38. Mattila PK, Batista FD, Treanor B. Dynamics of the actin cytoskeleton mediates receptor cross talk: an emerging concept in tuning receptor signaling. J Cell Biol 2016;212:267-80.

39. Ma CS, Wong N, Rao G, Avery DT, Torpy J, Hambridge T, et al. Monogenic mutations differentially affect the quantity and quality of T follicular helper cells in patients with human primary immunodeficiencies. J Allergy Clin Immunol 2015;136:993-1006.e1.

40. Molina IJ, Sancho J, Terhorst C, Rosen FS, Remold-O'Donnell E. T cells of patients with the Wiskott-Aldrich syndrome have a restricted defect in proliferative responses. J Immunol 1993;151:4383-90.

41. Engelhardt KR, McGhee S, Winkler S, Sassi A, Woellner C, Lopez-Herrera G, et al. Large deletions and point mutations involving the dedicator of cytokinesis 8 (DOCK8) in the autosomal-recessive form of hyper-IgE syndrome. J Allergy Clin Immunol 2009;124:1289-302.e4.

42. Mace EM, Orange JS. Lytic immune synapse function requires filamentous actin deconstruction by coronin 1A. Proc Natl Acad Sci U S A 2014;111:6708-13.

43. Candotti F. Clinical manifestations and pathophysiological mechanisms of the Wiskott-Aldrich syndrome. J Clin Immunol 2018;38:13-27.

44. Vandenberghe P, Beel K. Severe congenital neutropenia, a genetically heterogeneous disease group with an increased risk of AML/MDS. Pediatr Rep 2011;3(suppl 2):e9.

45. Hauck F, Voss R, Urban C, Seidel MG. Intrinsic and extrinsic causes of malignancies in patients with primary immunodeficiency disorders. J Allergy Clin Immunol 2018;141:59-68.e4.

METHODS
Case reports

Patient P1 (8 years old, male sex) born to consanguineous parents was admitted to the hospital with fever, diarrhea, aphthous stomatitis, and pneumonia at 8 years of age. Past medical history revealed that he had recurrent fever with vomiting, diarrhea, aphthous stomatitis, and hypokalemia occurring every 4 to 6 months, and although anti-thrombocyte antibodies were not studied, he was given a diagnosis of chronic idiopathic thrombocytopenic purpura at 2.5 years of age. On physical examination, mild intellectual disability and muscle weakness with positive Gowers sign were noted. Laboratory investigations showed chronic thrombocytopenia and an acute decrease in lymphocyte counts with increased neutrophil counts and acute-phase reactants during febrile episodes, which were triggered by infections every 4 to 6 months. *Candida albicans* was isolated from his aphthous lesions. Low IgG levels with B-cell lymphopenia were observed (Table II). Anti-rubella, anti-tetanus, and anti-diphtheria antibodies were positive, and results for anti-HB antibodies were negative. Anti-thyroglobulin and anti-TPO autoantibody results were also positive. At age 8 years, the Wechsler Intelligence Scale for Children–Revised test performed for evaluation of mental development and revealed a verbal IQ score of 72, a performance IQ score of 84, and a total IQ score of 75. Cranial magnetic resonance imaging results were normal, and results of muscle biopsy was consistent with noninflammatory myopathy. During follow-up, he responded well to fluconazole and trimethoprim-sulfamethoxazole prophylaxis with intravenous immunoglobulin replacement. The patient is currently stable and is being evaluated for bone marrow transplantation.

Patient P2 (12 years old, female sex) was admitted to the hospital with fever, growth retardation, and finger abscess at age 8 years. Past medical history was significant for recurrent pneumonia, bronchiectasis, aphthous stomatitis, and viral encephalitis. Having consanguineous parents, her family history revealed that she had 2 brothers with the same symptoms (Fig 1, *E*). She exhibited dysmorphic facial features, including frontal bossing, hypertelorism, and wide nostrils. Severe growth retardation was noted on physical examination, but growth hormone levels were normal. Leukocytosis and anemia were detected by using a complete blood count. Immunophenotyping revealed B-cell lymphopenia. The immunoglobulin levels were within age references (Table II). Prophylactic antibiotics and intravenous immunoglobulin replacement were initiated because she had severe recurrent infections at age 9 years. During follow-up, she had multiple episodes of hospitalizations and hepatosplenomegaly and lymphadenopathies with increased acute-phase reactant levels (see Table E2). A corresponding biopsy revealed reactive lymphoproliferation. Currently, she receives intravenous immunoglobulin and prophylactic antibiotics with apparently milder symptoms with growing age.

Patients P3 (21 years old, male sex) and P4 (24 years old, male sex) are brothers of P2. P3 was evaluated at age 18 years at the dermatology unit because of disseminated ulcerated lesions in the lower extremities that appeared 7 years previously after an episode of trauma. He had facial cystic acnes, a short stature, and difficulty in communication. Skin biopsy was compatible with pyoderma, but results of pustule cultures were negative. Laboratory assessment showed low IgM levels, B-cell lymphopenia, persistent leukocytosis with neutrophilia, high C-reactive protein and serum amyloid A levels (see Table E2), and fluctuating thrombocytopenia (Table II). Thorax computed tomography revealed bronchiectasis (data not shown). After starting regular intravenous immunoglobulin and Colchicum-Dispert, skin lesions improved, as did facial acne. P4 was admitted to the dermatology department at age 22 years with disseminated ulcerating purple-colored lesions causing pruritus developing on the tibial area 7 years before after trauma. Multiple cystic acne was also present on the face. Biopsy from the lesions revealed *Pyoderma gangrenosum*, and cultures were negative for bacteria and fungi. Bronchiectasis was detected on thorax computed tomography. He had the same laboratory abnormalities as his younger brother, lymphopenia, and persistent leukocytosis with polymorphonuclear leukocyte increase. Fluctuating thrombocytopenia with large platelet volume was recorded. Immunologic assessment revealed low B-cell numbers. Low IgM and IgG_2 levels were detected (Table II). He had persistent C-reactive

protein and serum amyloid A increases (see Table E2). Multiple antibiotic courses and dressings with intravenous immunoglobulin were administered. After beginning regular intravenous immunoglobulin (500 mg/kg) and Colchicum-Dispert, lesions were alleviated.

Patient P6 (7 years old, female sex) was born to consanguineous parents. She presented with recurrent febrile episodes every 1 to 2 months after a respiratory tract infection, together with generalized vesiculopustular lesions. Dermatologic evaluation and subsequent biopsy revealed subcorneal pustular dermatosis. She also had recurrent aphthous stomatitis and pneumonia, during which levels of acute-phase reactants remained high. Immunologic evaluation was significant for high IgA levels and low B-cell counts. She had generalized necrotic dermal lesions during the disease course. We lately discovered that her mother (patient P5 [26 years old, female sex]) had similar symptoms as her daughter. She experienced recurrent aphthous stomatitis, skin abscesses, and pneumonia.

Neutrophil mitochondrial membrane potential

Neutrophils were isolated from peripheral blood and cultured at low density in complete RPMI medium. As a measure of mitochondrial fitness, dissipation of its membrane potential was monitored by loss of JC-1 mitochondrial aggregates (red channel; excitation/emission, 535/590 nm) and a shift toward its monomeric cytosolic form (green channel; excitation/emission, 485/530 nm). Neutrophils were loaded with JC-1 dye (3.5 μmol/L; Life Technologies) at 37°C for 15 minutes, washed with PBS, and analyzed by using flow cytometry at the indicated time points. Gates were applied on intact and single cells based on forward- and side-scatter features.

Neutrophil apoptosis

Apoptosis was measured in neutrophils on spontaneous progression of cell death. At the indicated time points, cells were stained on ice with Annexin V–APC (3 μL per 100 μL; BD Biosciences) and propidium iodide (1.5 μL per 100 μL; BioLegend) in Annexin V binding buffer (eBioscience) for 5 minutes, topped up with an additional 200 μL of binding buffer, and kept on ice for acquiring by means of flow cytometry. Gates were defined by comparing with apoptotic control samples treated at 65°C for 10 minutes.

WDR1 expression in expanded T cells

Expanded T cells from patients and healthy donors were lysed in 100 μL of RIPA buffer. WDR1 expression was analyzed as described in the main Methods section.

TCR downregulation

P815 cells were coated with OKT3 at the indicated concentrations. $CD8^+$ T cells were purified with immunomagnetic beads and incubated with P815 cells at a 1:2 ratio for 4 hours. Cells were then stained with APC-H7–conjugated anti-CD3 and FITC-conjugated anti-TCR antibodies (BD Biosciences) for 30 minutes at 4°C. Expression of TCR at the $CD8^+$ T-cell surface was analyzed by using a Fortessa flow cytometer (BD Biosciences) and FlowJo software.

T-cell proliferation

PBMCs were labeled with eFluor 450 violet proliferation dye (BD Biosciences), according to the manufacturer's instructions. T-cell proliferation was assessed after 72 hours of stimulation with either soluble anti-CD3 antibody (1 μg/mL, clone OKT3; eBioscience) plus anti-CD28 antibody (1 μg/mL, clone CD28.2; eBioscience) or anti-CD3/CD28 antibody–coated Dynabeads (Sigma-Aldrich). Dilution of the proliferation dye was recorded on a BD Fortessa cytometer and analyzed with FlowJo X software.

T-cell migration

Ninety-six-well transwell plates (5-μm pore size; Corning) were used to assess T-cell migration in response to CXCL12. Expanded T cells were harvested and resuspended in serum-free RPMI 0.5% BSA medium at 0.5×10^6 cells/mL. Fifty microliters of cell suspension was loaded on the top of the transwell filter, whereas 150 μL of CXCL12 (PeproTech, Rocky

Hills, NJ) solution was added to the lower chamber at the indicated concentrations. After 4 hours of incubation at 37°C, transmigrating cells were collected and analyzed as described in the main Methods section.

T cell–mediated cytotoxicity

Green fluorescent protein–expressing P815 target cells pretreated with aphidicolin (Sigma-Aldrich) to prevent proliferation were coated with OKT3 at the indicated concentrations to assess $CD8^+$ T-cell cytotoxic function. $CD8^+$ T cells purified with immunomagnetic beads (MagniSort Human $CD8^+$ T-cell Enrichment Kit) were added to the green fluorescent protein–P815 target cells at a ratio of 1:1 for 4 or 24 hours, as indicated. After incubation, 150 μL of the respective cell suspensions was transferred to a 96-well plate, and 50 μL of a 10% 7-aminoactinomycin D solution (BD PharMingen) was added to each well. Analysis of residual target cell numbers was performed by using a Fortessa flow cytometer equipped with an automated plate reader device (BD Biosciences).

Chemotaxis of B-LCLs

Cells (10^5 B-LCLs in 6 μL of culture medium) were loaded into the central transversal channel of Ibitreat 3D Chemotaxis μ-slides (ibidi), coated with 5 μg/mL fibronectin, and incubated at 37°C for 30 minutes to allow cell attachment. A CCL19 gradient (0-200 ng/ml) was created, according to the manufacturer's instructions. Additional slides were prepared in parallel with a 10% dextran-FITC solution to verify gradient linearity and stability. Analysis of fluorescence intensity profiles showed that linear gradients were established within 3 hours and were stable over 24 hours. Slides were positioned in an Apotome microscope (Zeiss) equipped with a ×5/0.15 NA objective and with controlled temperature and CO_2 conditions. Recording of cell migration was initiated 5 hours after seeding and lasted for 14 hours at a rate of 1 image every minute. Obtained images were treated and binarized by using Image J software, and migration tracks were obtained by using the TrackMate plugin of the FIJI software. Only tracks lasting more than 20 minutes were considered. Chemotaxis plots and Forward Migration Index (FMI-Y) were obtained with the Chemotaxis and Migration tool from ibidi.
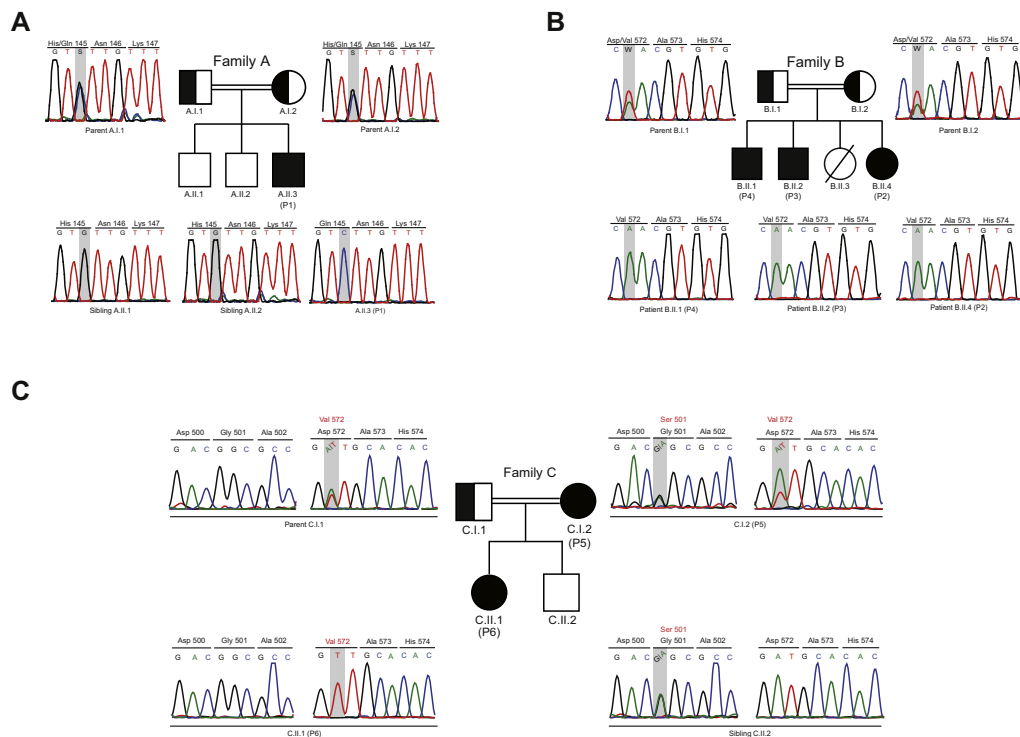
FIG E1. Segregation of *WDR1* variants in core pedigrees. **A,** Pedigree of family A and Sanger sequencing of *WDR1* at position 145-147. DNA sequences correspond to the antisense strand. **B,** Pedigree of family B and Sanger sequencing of *WDR1* at position 572-574. DNA sequences correspond to the antisense strand. **C,** Pedigree of family C and Sanger sequencing of WDR1 at positions 500-502 and 572-574. DNA sequences correspond to the sense strand.
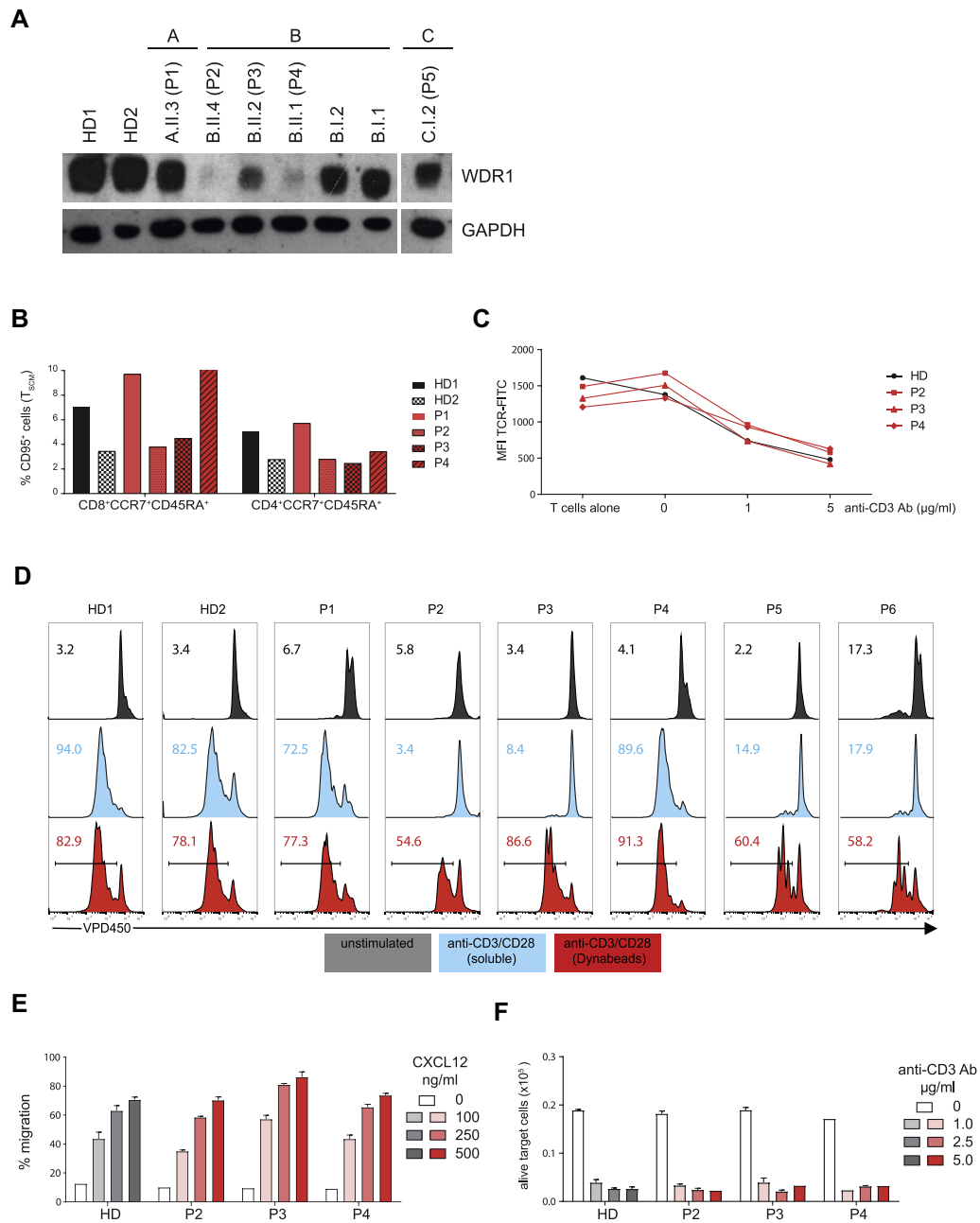
FIG E2. T-cell parameters in patients carrying *WDR1* variants. **A,** Representative Western blot analysis of WDR1 expression in lysates from expanded T cells derived from 2 healthy donors, patients P1 to P5, and parents of patients P2 to P4. Glyceraldehyde-3-phosphate dehydrogenase *(GAPDH)* is shown as a loading control. **B,** Flow cytometry–based quantification of the proportion of the stem memory T-cell subset in PBMCs from healthy donors and patients. **C,** TCR downregulation assessed by using flow cytometry after stimulation with the indicated concentrations of anti-CD3 antibody for 1 hour. **D,** Analysis of T-cell proliferation after 72 hours of stimulation of PBMCs with soluble anti-CD3/CD28 antibody or bead-coated anti-CD3/CD28 antibody. **E,** Proportion of expanded T cells that migrated in 4 hours across a transwell membrane in response to the indicated concentrations of CXCL12. **F,** Residual number of P815 target cells after 24 hours of incubation with purified CD8$^+$ T cells from a healthy donor and patients P1 to P4 at a 1:1 ratio. P815 cells had been coated previously with the indicated concentrations of anti-CD3 antibody to stimulate CD8$^+$ T-cell lytic activity. *HD,* Healthy donor.
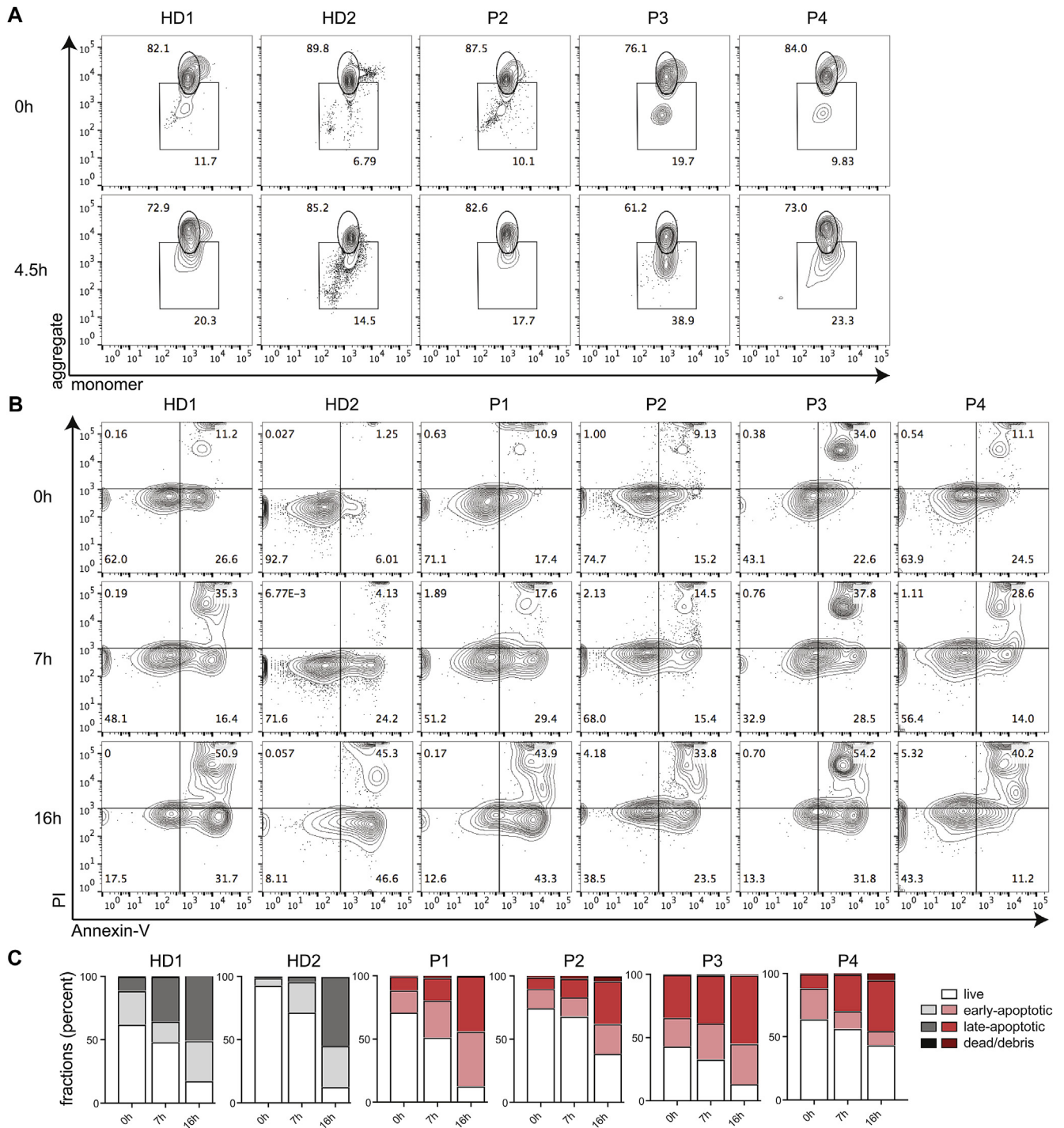
FIG E3. Mitochondrial membrane potential and apoptosis in neutrophils from patients carrying *WDR1* variants. **A,** Mitochondrial membrane potential monitored by using flow cytometric staining of JC-1 in neutrophils from 2 healthy donors and patients P2 to P4 on isolation and after 4.5 hours in complete RPMI medium. **B,** Apoptosis in neutrophils from 2 healthy donors and patients P1 to P4, as determined by staining for Annexin V and propidium iodide, after 0, 7, or 16 hours of incubation in complete medium. **C,** Quantification of apoptosis determined by staining for Annexin V and propidium iodide. *HD*, Healthy donor.
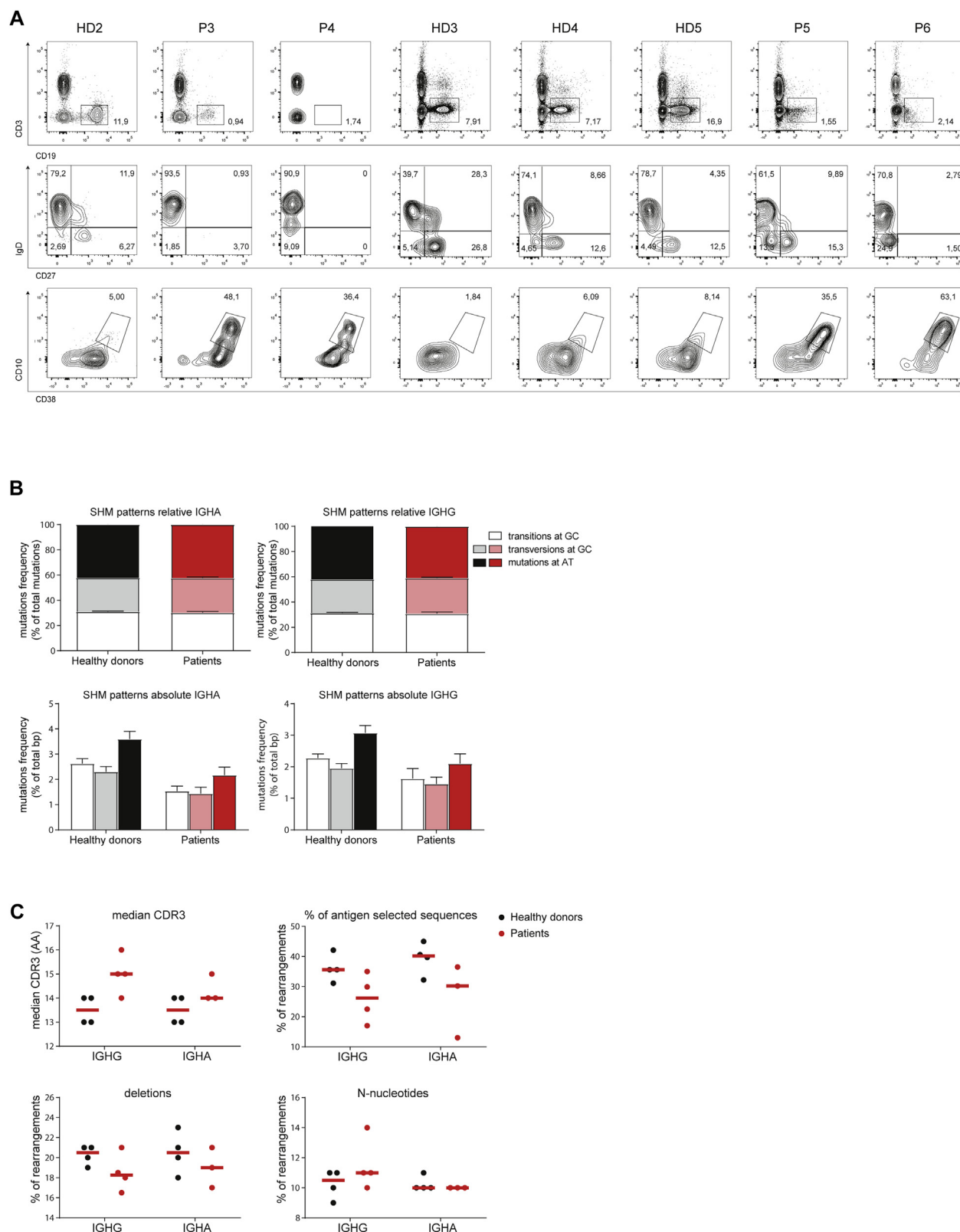
FIG E4. SHM patterns in B cells from patients carrying *WDR1* variants. **A,** Representative flow cytometric dot plots of the analysis of B-cell subsets in PBMCs from 4 healthy donors and patients P3 to P6. Data stem from 2 distinct experiments (experiment 1: HD2, P3, and P4; experiment 2: HD3 to HD5 and P5 to P6). **B,** Relative frequencies of transitions and transversions at GC and mutations at AT are shown as mean values for 4 healthy donors and patients P1 to P4. **C,** CDR3 length and proportions of antigen-selected sequences, deletions, and N-nucleotide rearrangements are shown for 4 healthy donors and patients P1 to P4.
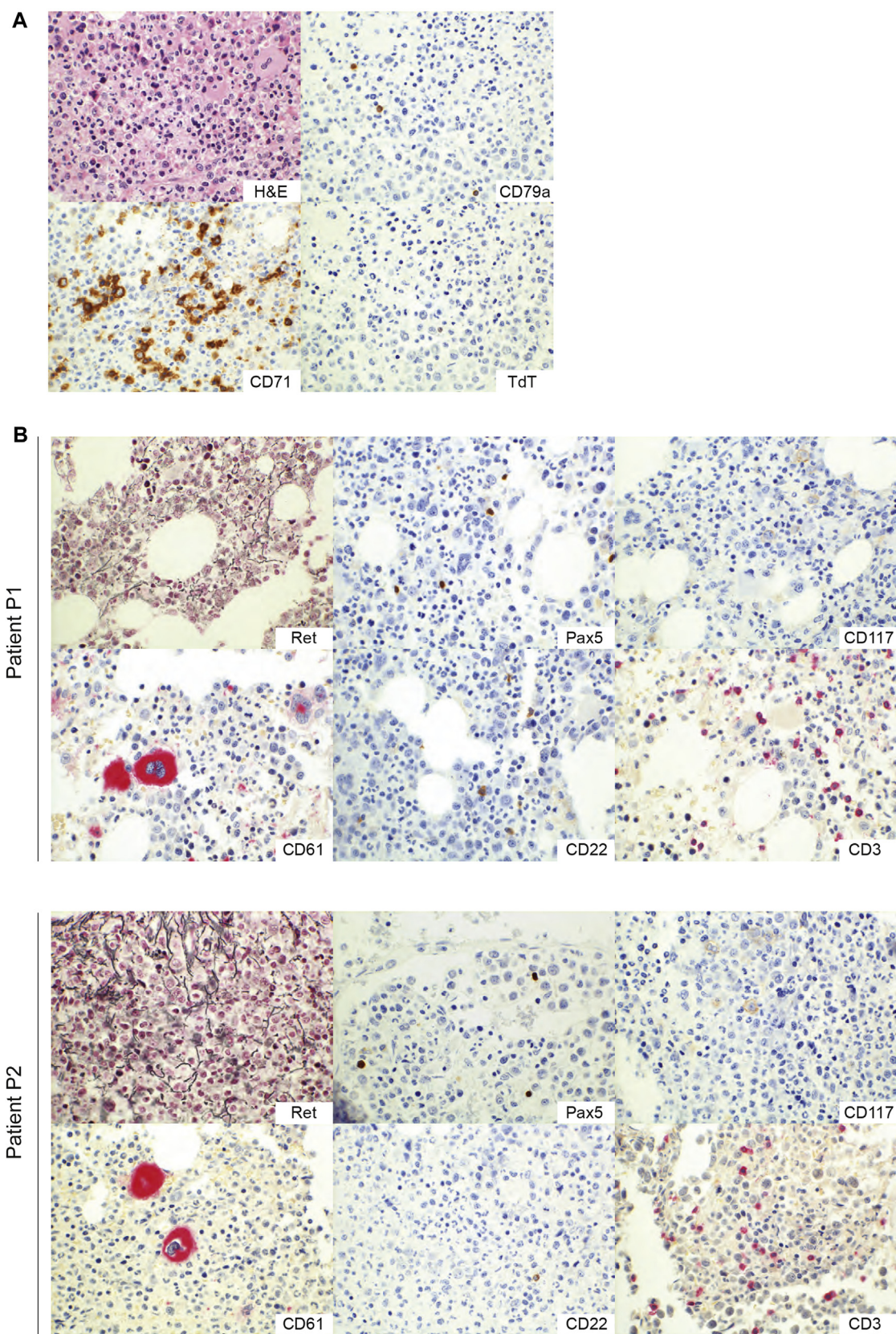
FIG E5. Bone marrow histology. **A,** Immunohistology staining for hematoxylin and eosin *(H&E)*, CD71, CD79a, or terminal deoxynucleotidyl transferase *(TdT)* in the bone marrow from patient P2. **B,** Immunohistology staining for reticulin *(Ret)*, Pax5, CD117, CD61, CD22, and CD3 in bone marrow from patients P1 and P2.
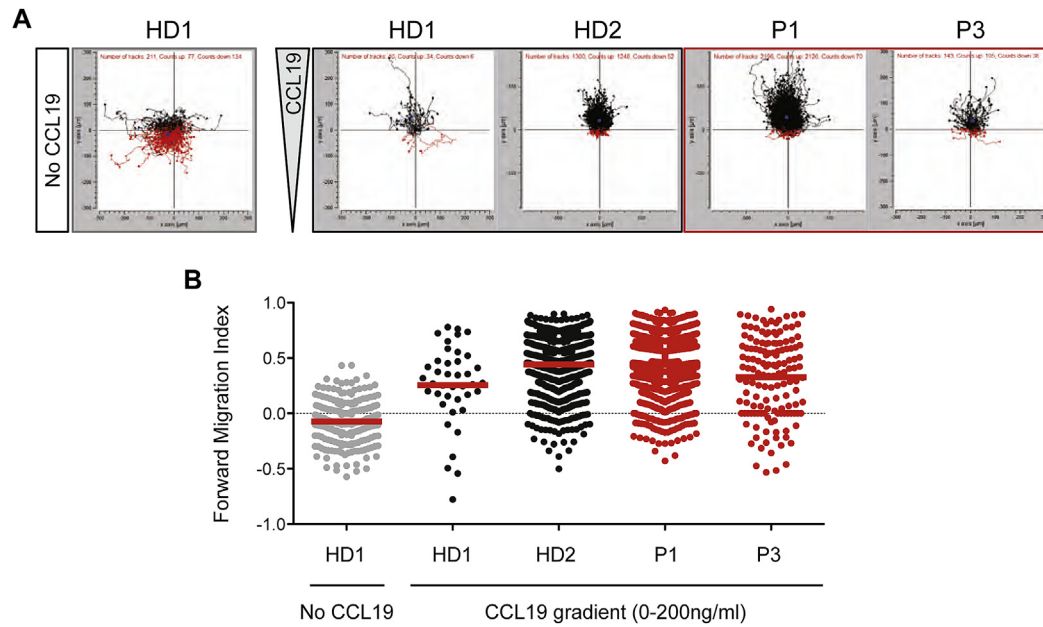
FIG E6. Migration toward CCL19 in B-LCLs from patients carrying *WDR1* variants. **A,** Tracks of B-LCLs from 2 healthy donors and patients P1 and P3 exposed to a gradient of CCL19. **B,** Directional migration of individual cells assessed as the forward migration index along the axis coincident with orientation of the CCL19 gradient.

TABLE E1. Hematologic values pertaining to anemia

| Family	A		B						C			
Patient	1		2		3		4		5		6	
Date	8/2014	3/2017	9/2014	8/2016	8/2014	3/2017	8/2014	3/2017	2/2016	12/2017	1/2016	12/2016
Hemoglobin (g/dL)	8.7	11.5	8.0	7.9	5.83	13.7	9.61	13.8	9.6	11.8	9.6	9.7
MCV (fL)	71.6	78.5	49	47.9	50.9	78.3	65.6	84.2	71.1	72.5	66	66.2
RDW (%)	13.8	15	24.6	23.1	20	13.9	18.5	13	16	15.5	19.9	18.9
Reticulocyte (%)	0.8	0.95	2.4	2	NA	NA	NA	NA	NA	NA	1.8	2
Direct coombs	Negative	Negative	Negative	Negative	NA	Negative	NA	NA	NA	NA	Negative	Negative
Ferritin (ng/mL)	NA	37.5	11.8	13.1	6.23	66.11	22	83	NA	NA	28.9	NA
Total iron (μg/dL)	16	51	6	8	12	47	13	24	NA	NA	12	NA
Total iron-binding capacity (μg/mL)	169	398	264	303	395	380	273	304	NA	NA	295	NA
Transferrin saturation (%)	NA	NA	2	2	3	12.3	4.7	7.8	NA	NA	4	NA

NA, Not available/applicable; *RDW*, red cell distribution width.

TABLE E2. Febrile episodes and concomitant biological parameters in patients 1, 2, and 6

Family	A		B		C	
Patient	1		2		6	
Date	2/2014	1/2017	9/2014	12/2016	1/2016	12/2016
Body temperature during representative febrile episodes (°C)	38.5	38.8	38.0	39.0	38.5	38.2
Leukocyte count (cells/μL)	20,330 (4,500-10,500)	18,460 (4,500-10,500)	15,410 (4,500-10,500)	13,910 (4,500-10,500)	13,910 (4,500-10,500)	24,820 (4,500-10,500)
Lymphocyte count (cells/μL)	830 (1,500-7,000)	1,250 (1,500-7,000)	4,230 (1,500-7,000)	1,360 (1,500-7,000)	1,360 (1,500-7,000)	1,420 (1,500-7,000)
Neutrophil count (cells/μL)	18,020 (1,500-8,000)	15,810 (1,500-8,000)	9,860 (1,500-8,000)	11,670 (1,500-8,000)	11,670 (1,500-8,000)	22,470 (1,500-8,000)
Hemoglobin	9.7 (11-16)	13 (11-16)	8.6 (11-16)	7.6 (11-16)	9.6 (11-16)	11.3 (11-16)
Thrombocyte count (cells/μL)	27,000 (15,000-400,000)	47,000 (15,000-400,000)	284,000 (15,000-400,000)	406,000 (15,000-400,000)	213,000 (15,000-400,000)	117,000 (15,000-400,000)
Ferritin (ng/mL)	236 (7-140)	347 (7-140)	11.8 (7-140)	20.1 (7-140)	28.9 (7-140)	NA
Fibrinogen (mg/dL)	575 (200-400)	NA	NA	405 (200-400)	281 (200-400)	NA
SAA (mg/L)	140 (0-6)	>216 (0-6)	NA	190 (0-6)	12.8 (0-6)	190 (0-6)
CRP (mg/dL)	12 (<0.5)	5.5 (<0.5)	8.23 (<0.5)	14.9 (<0.5)	10.24 (<0.5)	14.09 (<0.5)
Erythrocyte sedimentation rate (mm/h)	55	100	39	28	67	91
Specific clinical features accompanying febrile episodes	Aphthous stomatitis, diarrhea	Aphthous stomatitis, diarrhea, vomiting	Pneumonia, otitis media, common skin abscess	Pneumonia, otitis media, typhlitis, aphthous stomatitis	Bullous skin lesions, pneumonia	Bullous skin lesions, aphthous stomatitis, pneumonia

Values in parentheses indicate normal ranges. Patients 3, 4, and 5 did not present with febrile episodes during the current clinic follow-up. Data pertaining to the occurrence of previous episodes are not available.

CRP, C-reactive protein; *NA*, not available/applicable; *SAA*, serum amyloid A.

TABLE E3. Homozygous genetic variants segregating within families 1 and 2 together with *WDR1* mutations

Gene	Chromosome	Genomic position	SNP ID	R	A	AA	CADD	Biological function/phenotypic effect	Variant in previous reports
Family A									
WDR1	4	10099458		G	C	H145Q	13.3	—	—
WFS1	4	6302816	rs35031397	C	G	L432V	23.7	Wolfram syndrome-1 is a rare and severe autosomal recessive neurodegenerative disease characterized by diabetes mellitus, optic atrophy, diabetes insipidus, and deafness (DIDMOAD). Additional clinical features can include renal abnormalities, ataxia, dementia or mental retardation, and diverse psychiatric illnesses.	Variant found in heterozygosity in patients with diabetes and deafness (*WFS1* mutations in Spanish patients with diabetes mellitus and deafness)*
MTMR1	X	149895690	rs376319087	A	G	K119R	22.1	MTMR1 might play a role in muscle formation and might represent another target for abnormal mRNA splicing in myotonic dystrophy.	—
CLDN25	11	113650613		G	T	Q32H	10,15	This gene encodes a member of the claudin family. Claudins are integral membrane proteins and components of tight junction strands. Tight junction strands serve as a physical barrier to prevent solutes and water from passing freely through the paracellular space between epithelial or endothelial cell sheets and also play critical roles in maintaining cell polarity and signal transductions.	—
BLID	11	121986544		T	C	I29M	0.008	BLID functions as a proapoptotic molecule through the caspase-dependent mitochondrial pathway of cell death.	—
OTOP1	4	4199758	rs145349079	T	C	Y268C	23.8	This gene encodes a transmembrane protein that belongs to the otopetrin domain protein family and is required for formation of otoconia and otoliths, calcium carbonate biominerals within the inner ear of mammals that are required for detection of linear acceleration and gravity.	—
CPSF1	8	145624679		G	C	T460S	8.967	Cleavage and polyadenylation specificity factor (CPSF) is a multisubunit complex that plays a central role in 3-prime processing of pre-mRNAs.	-
Family B									
WDR1	4	10077108		T	A	D572V	28	—	—
TM4SF19	3	196054442	rs188688105	G	A	T7M	2.304	The protein encoded by this gene is a member of the 4-transmembrane L6 superfamily. Members of this family function in various cellular processes, including cell proliferation, motility, and adhesion through their interactions with integrins. In human brain tissue this gene is expressed at high levels in the parietal lobe, occipital lobe, hippocampus, pons, white matter, corpus callosum, and cerebellum.	—

A, Alternative base; *AA*, amino acid substitution; *R*, reference base; *SNP ID*, reference single nucleotide polymorphism number.
*Domenech et al, Eur J Hum Genet 2002;10:421-6.